Micromechanics and numerical modelling of the hydrogen–particle–matrix interactions in nickel-base alloys

Micromechanics and numerical modelling of the hydrogen–particle–matrix interactions in nickel-base alloys

Y Liang and P Sofronis[1]

Department of Theoretical and Applied Mechanics, University of Illinois at Urbana-Champaign, 104 S. Wright Street, Urbana, IL 61801, USA

E-mail: sofronis@uiuc.edu

Abstract

The mechanics of hydrogen-induced decohesion and subsequent void formation at the interface of an elastic inclusion embedded in a ductile matrix is studied in an effort to understand the micromechanics of hydrogen embrittlement in nickel-base alloys that fail by ductile intergranular fracture initiating at grain boundary carbides. A phenomenological decohesion model calibrated with the use of the thermodynamic theory of Rice (1976), Hirth and Rice (1980), and Rice and Wang (1989) at its 'fast-separation limit' is employed to describe the cohesive properties of the inclusion/matrix interface in the presence of hydrogen. Finite element solution to the transient hydrogen transport through the plastically deforming matrix, the elastic inclusion, and the decohering interface coupled with interfacial debonding and large-strain deformation in the surrounding matrix is obtained incrementally at a unit cell through an updated Lagrangian formulation scheme. The numerical results are used to analyse: (a) the interaction of hydrogen-induced decohesion with hydrogen-induced matrix softening; (b) the relationship between energy expenditures on bulk deformation and interfacial decohesion; and (c) the importance of parameters such as strain rate and relative magnitude between interfacial and bulk diffusivities on void nucleation at the particle/matrix interface. For material data pertaining to alloy 690, it was found that hydrogen by weakening the interface promotes plastic flow localization in the surrounding matrix. In general, hydrogen was found to decrease both the macroscopic stress and strain at which void initiation commences and reduce the energies expended on bulk deformation and interfacial separation.

[1] Author to whom correspondence should be addressed.

1. Introduction

Low temperature (<150°C) environmental degradation of nickel-base alloys 690 and X-750 in both pressurized water and boiling water nuclear reactors appears to be a hydrogen embrittlement phenomenon manifested in precipitous drop of fracture toughness and rapid subcritical crack growth (Grove and Petzold 1985). The fracture morphology of hydrogen-charged cylindrical tensile or notched bend specimens consists of fine intergranular dimples, and the predominantly intergranular fracture mechanism is microvoid initiation at grain boundary carbides ($\sim 1 \mu$m) followed by growth and coalescence (Symons and Thomspon 1996, 1997, Symons 1998).

Young and Scully (1997) have demonstrated experimentally that carbides at grain boundaries trap hydrogen at the carbide/matrix interface in Ni–Cr–Fe alloys. Studying the fracture behaviour of alloy X-750, Symons and Thomspon (1996) concluded that at 25°C diffusion can provide local hydrogen enrichment at grain boundaries. It was then envisioned that the role of hydrogen trapped at the carbides is to reduce the cohesion of the carbide/matrix interface by reducing the effective surface energy (Thompson and Knott 1993) that is the sum of the surface energy and the plastic energy used in creating the new surfaces. Thus, Symons and Thomspon (1996, 1997) suggested that the role of hydrogen was to decrease the strain to nucleate voids at the $M_{23}C_6$ carbides decorating the grain boundaries and that the void growth process might not be significantly altered by hydrogen. Investigating the effect of hydrogen on the fracture behaviour of alloy 690, Symons (1998) came up with clear fractographic evidence that in hydrogen-charged specimens the intergranular cracks run through the carbide/matrix interface (figure 1). He also observed that the degree of embrittlement was increased as the material was aged. The explanation is that aging provides a larger number of grain boundary carbides acting as hydrogen traps, thereby increasing the number of potential decohesion sites.

It is evident from the above discussion that in order to understand the mechanistic effect of hydrogen on the fracture behaviour of the Ni–Cr–Fe alloys discussed, one needs to focus on the micromechanics of hydrogen interactions between the matrix/carbide interface and the elastoplastically deforming matrix. In other words, one needs to adopt the viewpoint that interfacial decohesion by bond breaking is concomitant with dislocation activity around the decohering interface. Experimental evidence for concurrent localized plasticity and intergranular fracture has also been observed in other systems such as iron and steels (by way of example one can mention the following investigations: Oriani and Josephic (1974, 1977, 1979), Lessar and Gerberich (1976), Briant *et al* (1978), Takeda and McMahon (1981), Bandyopadhyay *et al* (1983), Morgan (1987), Gerberich and Foecke (1990), Chen *et al* (1990), Chen and Gerberich (1991), Chen *et al* (1991), McMahon (2001)). In particular, Gerberich *et al* (1991) spoke on the necessity of both plasticity and brittleness in the fracture threshold of iron; and Takeda and McMahon (1981) based on their experimental observations in steels termed hydrogen-induced failures as plasticity related hydrogen-induced cracking. Symons (2001) comparing internal and environmental hydrogen embrittlement of X-750 suggested that local hydrogen accumulations at grain boundaries promote decohesion whereas hydrogen accumulations over large regions ahead of a notch may enhance plasticity. Further experimental evidence on the simultaneous operation of decohesion and plasticity in promoting fractures considered to be macroscopically brittle can be found in the work of Jokl *et al* (1980).

It should be mentioned that although the hydrogen effect separately on decohesion (e.g. Van Leeuwen (1974), Gerberich and Chen (1975), Unger (1989), Chen and Gerberich (1991), Gerberich *et al* (1991)) and plasticity (e.g. Sato and Meshii (1973), Tobe and Tyson (1977), Onyewuenyi and Hirth (1982, 1983), Rajan and Hirth (1987), Hirth (1990), Birnbaum (1994), Sofronis *et al* (2001)) has been modelled in the past, no systematic effort has
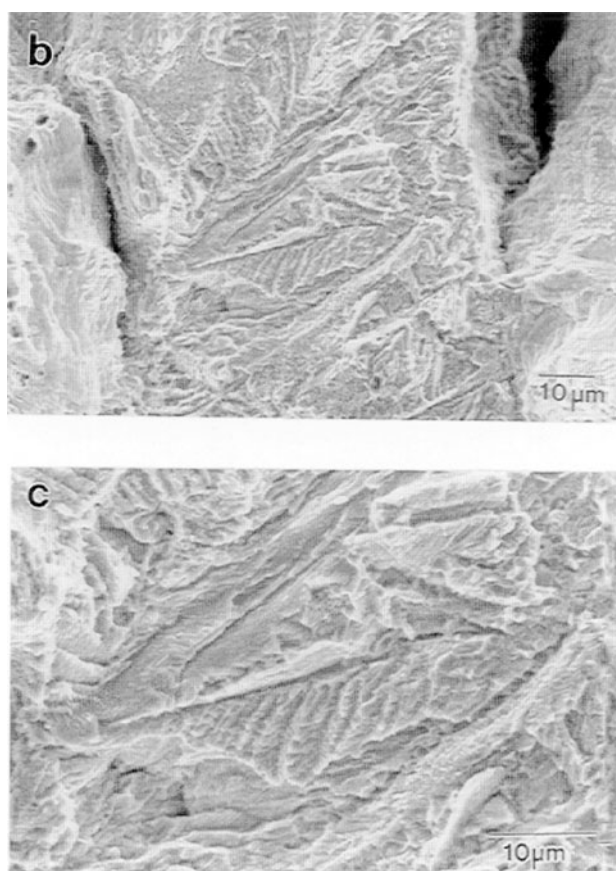
Figure 1. Fractography of hydrogen-charged tensile specimen with 38 wppm of H. The grain faces appear to have the outline of dendritic carbides on the fracture surface (figures 8(*b*) and (*c*) from Symons (1998), with permission from ASM International and the Minerals, Metals and Materials Society).

been made to date to model simultaneously the effects of hydrogen on interfacial decohesion and bulk plasticity in a boundary-value problem setting in which hydrogen is transported in a transient mode and interfacial decohesion takes place in mechanical equilibrium with stresses in the surrounding bulk material. A serious effort in the direction of modelling impurity-induced intergranular cracking is the work of Xu and Bassani (1999) who modelled simultaneously the impurity diffusion mechanism, the time-dependent crack tip stress field, and the effect of impurities on interface strength in a cohesive zone framework ahead of a propagating crack at steady-state in a Cu–Sn alloy. Mishin *et al* (2002) introduced a new theory of decohesion by solute impurities extending that of Hirth and Rice quantitatively into intermediate separation regimes, and studied the kinetics of interfacial decohesion under uniform stress. Very recently, the present authors (2002) suggested a phenomenological traction–separation law that accounts for hydrogen effects and can be readily implemented to describe the constitutive response of cohesive finite element to simulate interfacial decohesion (Needleman 1987). At fast decohesion, the law yields a reversible work of separation which is identical to that predicted by the thermodynamic theory of Rice (1976), Hirth and Rice (1980), and Rice and Wang (1989).

To address the questions raised above, an effort is made in this paper to simulate the effect of hydrogen on particle/matrix interfacial decohesion in conjunction with the effect of hydrogen on material elastoplasticity in a unit cell that contains an elastic inclusion embedded in a ductile matrix and deforms under plane-strain conditions. Prior to the application of the load, hydrogen is assumed to be at an initial hydrogen concentration that is established in the material usually during charging in a high-pressure hydrogen autoclave. In view of the periodic coverage of the grain boundaries by carbides, the boundaries of the cell were assumed to be insulated. Once the load was applied, transient hydrogen transport through the matrix, the inclusion, and the matrix/inclusion interface was monitored in time in a coupled fashion with material deformation and interfacial decohesion. The mechanics of interfacial decohesion was dealt with through the cohesive-element methodology developed by Needleman (1987), Tvergaard (1990), and Tvergaard and Hutchinson (1993) with a hydrogen-affected interfacial traction–separation law as described in the work of Liang and Sofronis (2003). The hydrogen effect on matrix elastoplasticity was treated as in the work of Sofronis *et al* (2001) who based on the experimental observations of Robertson and co-workers (Tabata and Birnbaum 1983, 1984, Robertson and Birnbaum 1986, Bond *et al* 1987, 1988, Rozenak *et al* 1990, Eastman *et al* 1981, Teter *et al* 2001) postulated that hydrogen reduces the flow stress of the material in a local small volume and this reduction is proportional to the corresponding local hydrogen concentration in the material. The objectives of the paper are to: (i) study the role of solute hydrogen on the initiation of interfacial debonding and the subsequent propagation of the interfacial debond length coupled with material elastoplasticity; (ii) determine the effect of hydrogen on the energy expenditures on interfacial decohesion and matrix deformation; (iii) establish whether hydrogen affects the macroscopic stress or strain for void nucleation and quantify the effect; and (iv) find whether there is any competitive or synergistic action between hydrogen-induced decohesion and material softening in promoting void nucleation or plastic shear localization.

2. The hydrogen transport model

2.1. Transport in a solid strained elastoplastically

According to the hydrogen transport model of Johnson and Lin (1982), Sofronis and McMeeking (1989), and Krom *et al* (1999) one can assume that hydrogen resides either at normal interstitial sites (NILS) or reversible trapping sites generated by plastic deformation. The two populations are always in equilibrium according to Oriani's theory (1970), such that

$$\frac{\theta_T}{1 - \theta_T} = \frac{\theta_L}{1 - \theta_L} \exp\left(\frac{W_B}{RT}\right), \tag{1}$$

where θ_L denotes the occupancy of the NILS, θ_T denotes the occupancy of the trapping sites, W_B is the trap binding energy, R is the gas constant equal to $8.31\,\mathrm{J\,mole^{-1}\,K^{-1}}$ and T is the absolute temperature. The hydrogen concentration measured in H atoms per unit volume in trapping sites, C_T, can be phrased as

$$C_T = \theta_T \alpha N_T, \tag{2}$$

where α denotes the number of sites per trap and N_T, which is a function of the local effective plastic strain, i.e. $N_T = N_T(\varepsilon^p)$, denotes the trap density measured in number of traps per unit volume. The hydrogen concentration measured in H atoms per unit volume in NILS, C_L, can be stated as

$$C_L = \theta_L \beta N_L, \tag{3}$$

where β denotes the number of NILS per solvent atom and N_L denotes the number of solvent lattice atoms per unit volume and is given by $N_L = N_A/V_M$, in which V_M is the molar volume

of the host metal lattice measured in units of volume per mole and $N_A = 6.0232 \times 10^{23}$ atoms per mole is Avogadro's number. Hydrogen conservation in any arbitrary material volume combined with equations (1) through (3) yields the governing equation for transient hydrogen diffusion accounting for trapping and hydrostatic drift as

$$\frac{D}{D_{eff}} \frac{dC_L}{dt} - DC_{L,ii} + \left(\frac{DV_H C_L}{3RT} \sigma_{kk,i} \right)_{,i} + \alpha \theta_T \frac{\partial N_T}{\partial \varepsilon^p} \frac{d\varepsilon^p}{dt} = 0, \tag{4}$$

where $(\ )_{,i} = \partial (\ )/\partial x_i$, d/dt is the time derivative, D is the hydrogen diffusion constant through NILS, $D_{eff} = D/(1 + \partial C_T/\partial C_L)$ is an effective diffusion constant that varies pointwise depending on the trapping site populations, V_H is the partial molar volume of hydrogen in solid solution, σ_{ij} is the Cauchy stress, and the standard summation convention over the range from 1 to 3 is implied for a repeated index. Clearly, equation (4) demonstrates that the calculation of the hydrogen distribution is coupled to the fields of the hydrostatic stress and effective plastic strain. In addition, as more traps are generated by continued plastic straining, the hydrogen populations in both NILS and traps change according to the dynamic model of hydrogen transport described by equations (1)–(4). In other words, this model does account for the fact that both NILS and trapping site occupancies continuously change with straining and hydrogen diffusion at any given location.

2.2. Transport along an internal decohering interface

The interface in the present solid mechanics model is the boundary between the particle and the matrix. Under load, the particle side of the interface begins to separate from the matrix side of the interface, while normal and tangential tractions are holding the two sides together as they separate (see section 4). It is assumed that interfacial hydrogen diffusion and trapping begins to take place in the space between the two sides once the separation process initiates. In other words, the material mechanism for accommodating interfacial diffusion is simulated through the separation process. Thus, in the absence of separation, there is no interfacial diffusion channel. The interface diffusion process begins to take place simultaneously with the bulk matrix- and particle-diffusion processes upon the application of the load, provided that the system is at a uniform initial concentration. It should also be mentioned that the tractions holding the two sides separated at any finite distance vanish when decohesion occurs, that is, after the separation reaches a critical value (see section 4).

Once the two sides of the particle/matrix interface begin to separate, hydrogen may diffuse into the interfacial channel and move along the interface toward points of lower chemical potential. It is assumed in this model that the interface provides sites through which interfacial hydrogen can diffuse and trapping sites at which hydrogen gets trapped (segregated). Thus, as in the case of the transport model though bulk material in which hydrogen diffuses through NILS and gets trapped at microstructural defects, it is analogously assumed that there are again two interfacial populations, namely diffusing hydrogen and trapped hydrogen.

To quantitatively model hydrogen transport through the interface in a way that can be coupled with equation (4) for the bulk material, the H atoms on the interface are assumed to be distributed uniformly in the interfacial thickness direction in the space created by the opening interface. The diffusing populations are denoted by C_L as in the case of hydrogen diffusing through bulk NILS and correspondingly the trapped populations are denoted by C_T. It is further assumed that the two populations are in equilibrium as dictated by equation (1) in which the trapping binding energy W_B is the corresponding binding energy to the interface. An infinitesimal element of an opening interface under plane-strain conditions is shown in figure 2. For the treatment of diffusion, it is assumed that the two opposite sides, upper S_+ and
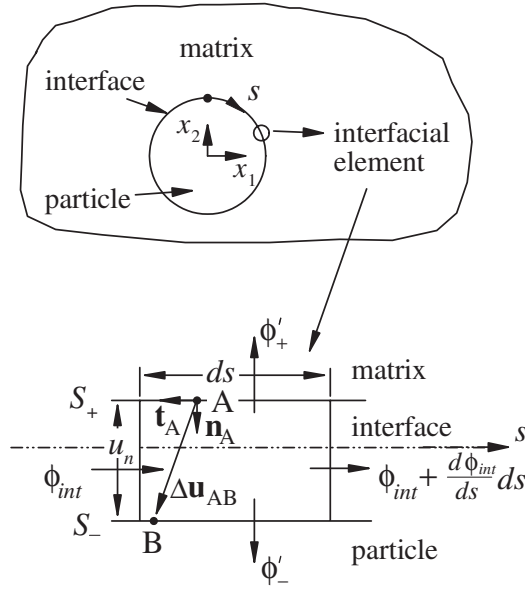
Figure 2. A schematic of an infinitesimal element of a separating interface. The parameters ϕ'_+ and ϕ'_- denote the hydrogen fluxes coming out of the interface through sides S_+ and S_-, respectively, ϕ_{int} is the hydrogen flux through the interfacial thickness u_n, and ds is the arclength. Vectors $\boldsymbol{n}_A$ and $\boldsymbol{t}_A$ are normal and tangential vectors of unit magnitude, and $\Delta\boldsymbol{u}_{AB}$ is the relative displacement between two points A and B that were coincident before separation.

lower S_-, are close enough to each other so that $du_n/ds \ll 1$, where $u_n(s)$ is the interfacial separation as a function of arclength s along the interface with $s = 0$ at the top of the particle. Hydrogen conservation along the interface requires

$$\frac{d}{dt}[(C_L + C_T)u_n] + \frac{d(\phi_{\text{int}}u_n)}{ds} + \phi'_- + \phi'_+ = 0, \tag{5}$$

where ϕ_{int} is the hydrogen flux along the interface through the thickness u_n, which continuously changes as the separation of the two interface sides progresses, and ϕ'_+ and ϕ'_- are the hydrogen fluxes away from the interface through the sides S_+ and S_-, respectively (figure 2). The hydrogen flux ϕ_{int} is related to the chemical potential gradient along the interface through

$$\phi_{\text{int}} = -\frac{D_{\text{int}}C_L}{RT}\frac{d\mu_{\text{int}}}{ds}, \tag{6}$$

where D_{int} is the interface diffusion coefficient,

$$\mu_{\text{int}} = \mu_0 + RT\ln\left(\frac{C_L}{C_L^0}\right) - T_n V_H \tag{7}$$

is the chemical potential of diffusing hydrogen along the interface, T_n is the normal Cauchy stress on the interface, and μ_0, which is a function of temperature, is the chemical potential at the initial NILS concentration C_L^0 in the absence of stress. Stress T_n is positive when it acts to separate the interface, thus decreasing the chemical potential algebraically.

It should be noted that for any interfacial segment that is completely debonded and the two sides are free of traction, the model assumes that diffusion driven by concentration gradients and trapping of hydrogen at the traps generated upon complete separation continues in the free space between the two sides.

3. Elastoplastic constitutive law in the presence of hydrogen

Birnbaum (1994), Birnbaum and Sofronis (1994), and Sofronis and Birnbaum (1995) have argued that at temperatures and strain rates in which hydrogen embrittlement is experimentally observed hydrogen induces material softening at the microscale by enhancing the dislocation mobility. A recent summary of the experimental evidence on hydrogen-enhanced dislocation mobility is given in the work by Robertson (2001). In a continuum sense, local material softening can be described through a local flow stress, σ_Y, that decreases with increasing hydrogen concentration (Sofronis *et al* 2001)

$$\sigma_Y(\varepsilon^p, c) = \sigma_0(c) F(\varepsilon^p) \tag{8}$$

in which $c = (C_L + C_T)/N_L$ is the total hydrogen concentration in NILS and trapping sites measured in H atoms per solvent atom, $\sigma_0(c)$ is the yield stress in the presence of hydrogen such that $\sigma_0(0) = \sigma_0$ is the yield stress in the absence of hydrogen and function $F(\varepsilon^p)$ describes strain hardening. A possible suggestion for $\sigma_0(c)$ is a linear form

$$\sigma_0(c) = [(\xi - 1)c + 1]\sigma_0, \tag{9}$$

where $\xi \leqslant 1$ is a softening parameter. Since the concentrations at which embrittlement of nickel-base alloys is observed are of the order of only 1000 appm, the parameter ξ can be chosen to be sufficiently negative to model pronounced hydrogen effects provided that $\sigma_0(c) > 0$. The proposed model of equations (8) and (9) for the hydrogen-induced material softening should be understood not as a precise and exhaustive description of the experimental findings. Rather, the model should be viewed as an attempt to quantify the experimental understanding of the hydrogen effect on dislocation mobility in a continuum sense.

The total deformation rate tensor (which is equal to the symmetric part of the velocity gradient) can be written as

$$D_{ij} = D_{ij}^e + D_{ij}^p + D_{ij}^h. \tag{10}$$

The elastic part of the deformation rate tensor, D_{ij}^e, is modelled as hypo-elastic, linear and isotropic:

$$D_{ij}^e = \frac{1}{2G} \overset{\nabla}{\sigma}{}'_{ij} + \frac{1}{9K} \overset{\nabla}{\sigma}_{kk} \delta_{ij}, \tag{11}$$

where the superposed ∇ denotes the Jaumann or co-rotational rate which exhibits proper material invariance for rigid rotation, $\sigma'_{ij} = \sigma_{ij} - \sigma_{kk}\delta_{ij}/3$ is the deviatoric stress, δ_{ij} is the Kronecker delta, and G and K are the elastic shear and bulk moduli, respectively.

The parameter D_{ij}^h denotes the deformation rate due to hydrogen-induced lattice straining and it is purely dilatational and isotropic (Peisl 1978):

$$D_{ij}^h = \frac{d}{dt}\left[\ln\left(1 + \frac{c - c_0^{tot}}{3}\lambda\right)\right]\delta_{ij}, \tag{12}$$

where c_0^{tot} is the initial hydrogen concentration in NILS and traps measured in hydrogen atoms per solvent atom, $\lambda = \Delta v/\Omega$, $\Delta v = V_H/N_A$ is the volume change per hydrogen atom introduced into solution, and Ω is the mean atomic volume of the host metal atom.

Assuming rate-independent plasticity, von Mises yielding, $f = \sigma_e - \sigma_Y(\varepsilon^p, c) = 0$ where $\sigma_e = \sqrt{3\sigma'_{ij}\sigma'_{ij}/2}$ is the effective stress, and isotropic hardening with plastic straining, one deduces that the associated flow rule is given by

$$D_{ij}^p = \frac{1}{\partial\sigma_Y/\partial\varepsilon^p}\left(\frac{3\sigma'_{kl}}{2\sigma_e}\overset{\nabla}{\sigma}_{kl} - \frac{\partial\sigma_Y}{\partial c}\dot{c}\right)\frac{3\sigma'_{ij}}{2\sigma_e}. \tag{13}$$

It is notable that as the hydrogen concentration changes, so does the plastic strain rate. Substituting equations (11)–(13) into equation (10) gives the material constitutive law in the presence of hydrogen as

$$\overset{\triangledown}{\sigma}_{ij} = 2G \left\{ \delta_{ik}\delta_{jl} + \frac{\nu}{1-2\nu}\delta_{ij}\delta_{kl} - \frac{3}{2}\frac{\sigma'_{ij}\sigma'_{kl}}{((h/3G)+1)\sigma_e^2} \right\}(D_{kl} - D_{kl}^{\mathrm{h}}) + \frac{3G}{h+3G}\frac{\sigma'_{ij}}{\sigma_e}\frac{\partial\sigma_Y}{\partial c}\dot{c}$$

(14)

in which ν is Poisson's ratio and $h = \partial\sigma_Y/\partial\varepsilon^{\mathrm{p}}$.

4. Interface decohesion

Decohesion at particle/matrix interfaces inevitably involves opening and shear. The latter is not well understood at the atomic level, but phenomenological models that account for both have been presented. In this work, the model of Liang and Sofronis (2003) is adopted to characterize the hydrogen effect on interfacial cohesion through a traction–separation law. According to this model, the normal and tangential components of the nominal traction T^0 (force/unit reference area) on the interface are given, respectively, by

$$T_n^0 = \frac{\sigma(q,\Gamma)}{q}\frac{u_n}{\delta_n}, \qquad T_t^0 = \frac{\sigma(q,\Gamma)}{q}\frac{\delta_n}{\delta_t}\frac{u_t}{\delta_t},$$

(15)

where

$$\sigma(q,\Gamma) = \frac{27\hat{\sigma}(\Gamma)q(1-q)^2}{4}, \qquad q = \sqrt{\left(\frac{u_n}{\delta_n}\right)^2 + \left(\frac{u_t}{\delta_t}\right)^2}$$

is a non-dimensional interfacial separation parameter such that the traction drops to zero when $q \geqslant 1$, $u_n = \boldsymbol{n}_A \cdot \Delta\boldsymbol{u}_{AB}$ and $u_t = \boldsymbol{t}_A \cdot \Delta\boldsymbol{u}_{AB}$ are, respectively, the components of the relative normal and tangential interfacial displacements in which $\Delta\boldsymbol{u}_{AB} = \boldsymbol{u}_B - \boldsymbol{u}_A$ is the relative displacement vector, $\boldsymbol{n}_A$ is the unit vector normal to the side at any point A pointing away from the matrix (figure 2), and $\boldsymbol{t}_A$ is the unit tangent vector at point A of the interface (coincident with point B before separation) as shown in figure 2. The parameter δ_n is a characteristic material constant such that for purely normal separation ($u_t = 0$, $q = u_n/\delta_n$) the traction $T_n^0 = \sigma(q,\Gamma)$ is different from zero only when $u_n < \delta_n$. Similarly, the parameter δ_t is a material constant such that for purely tangent separation ($u_n = 0$, $q = u_t/\delta_t$), the traction $T_t^0 = (\delta_n/\delta_t)\sigma(q,\Gamma)$ is different from zero only when $|u_t| \leqslant \delta_t$. The parameter Γ denotes the solute segregation (trapped hydrogen) at any point A of the interface (see figure 2) and is measured in H atoms per unit reference interfacial area. It is related to the interfacial trapped-hydrogen concentration C_T through $\Gamma = J_s u_n C_T$, where $J_s = \mathrm{d}S/\mathrm{d}S_0$ is the ratio of the current to the reference area element. In view of the lack of any direct experimental evidence, it was assumed in the model of equation (15) that it is only the hydrogen atoms trapped (segregated) onto the interface that affect the interfacial cohesive properties whereas mobile hydrogen atoms that diffuse along or through the interface have no effect. Under the assumption that there is no hydrogen effect on the maximum separation constants δ_n and δ_t, the model describes the role of hydrogen through the function $\hat{\sigma}(\Gamma)$ whose value $\hat{\sigma}(\Gamma = 0)$ in the absence of hydrogen denotes the maximum cohesive stress in purely normal separation.

Liang and Sofronis (2003) determined the function $\hat{\sigma}(\Gamma)$ by requiring that the reversible work of separation

$$2\gamma_{\mathrm{int}} = \int_0^{u_n^{\mathrm{sep}}} T_n^0 \,\mathrm{d}u_n + \int_0^{u_t^{\mathrm{sep}}} T_t^0 \,\mathrm{d}u_t = \delta_n \int_0^1 \sigma(q',\Gamma)\,\mathrm{d}q'$$
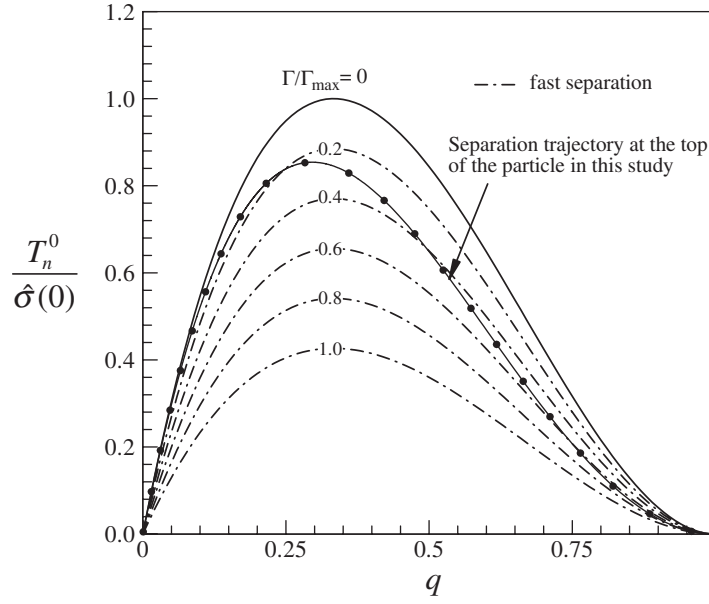
(16)

Figure 3. Normalized interfacial traction $T_n^0/\hat{\sigma}(0)$ versus separation parameter q for 'fast-separation' at various Γ/Γ_{max} and temperature 300 K. The separation trajectory of the top point of the particle in the present numerical simulation is also included. The parameter $\hat{\sigma}(0)$ denotes the interfacial cohesive strength in the absence of hydrogen.

at constant solute segregation Γ be equal to the corresponding work predicted by the thermodynamic theory of Rice (1976), Hirth and Rice (1980), and Rice and Wang (1989). In equation (16), $\sqrt{(u_n^{sep}/\delta_n)^2 + (u_t^{sep}/\delta_t)^2} = 1$, and u_n^{sep} and u_t^{sep} are, correspondingly, the normal and tangential relative displacements at separation. For the nickel-base alloy 690, this calibration yields

$$\frac{\hat{\sigma}(\Gamma)}{\hat{\sigma}(0)} = 1 - 0.4724 \left(\frac{\Gamma}{\Gamma_{max}} \right), \tag{17}$$

where $\Gamma_{max} = 2/a^2$, is the maximum interfacial segregation for octahedral site occupancy along the chromium carbide/fcc matrix interface [100], and $a = 3.58 \times 10^{-10}$ m is the lattice parameter. Thus, $\Gamma_{max} = 1.56 \times 10^{19}$ H atoms m^{-2}. Assuming that the maximum interfacial segregation, Γ_{max}, is attained when $u_n = \delta_n$ and $\theta_T = 1$, and using $\Gamma_{max} = u_n C_T$ ($J_s \approx 1$) along with $C_T = \alpha N_T \theta_T$, one finds $\Gamma/\Gamma_{max} = \theta_T u_n/\delta_n$ and $N_T = \Gamma_{max}/\alpha\delta_n = 2/\alpha a^2\delta_n$ (Liang and Sofronis 2003). In the decohesion model of equations (15) and (17), the segregation Γ varies with time as required by the hydrogen transport kinetics. Thus, even though the model has been calibrated at fast-separation conditions at which the segregation does not change with time, it addresses interfacial decohesion in a transient solute concentration mode. Figure 3 shows the normalized interfacial traction $T_n^0/\hat{\sigma}(0)$ under pure normal separation and calculated with the use of equation (17) plotted against separation $q = u_n/\delta_n$ at various interfacial segregations Γ/Γ_{max}. Also shown in the figure is the separation trajectory for the top point of the particle as determined by the finite element calculations in section 6.2. It is notable that the interfacial cohesion is markedly reduced with increasing hydrogen segregation despite the fact that model was calibrated at the fast-decohesion limit of the Hirth and Rice (1980) thermodynamics which is known not to yield dramatic cohesion reductions.

5. Finite element formulation

In this paper, the composite material (particle and matrix) behaviour was modelled by the response of a square unit cell occupying volume V bounded by surface S in the current configuration and subjected to external tractions $\boldsymbol{T}^{\text{sp}}$ on the part of the boundary S_{T} under plane-strain deformation conditions. Upon the application of tractions $\boldsymbol{T}^{\text{sp}}$ the particle/matrix interface begins to open up with the two forming sides termed S_+ and S_-, and the corresponding interfacial traction $\boldsymbol{T}$. The interfacial separation is both normal and tangential and is described by equations (15) and (17). In the absence of body forces, the equilibrium of the cell is stated in terms of the principle of virtual velocities as

$$G(\boldsymbol{u}, \boldsymbol{v}^*) = \int_V \boldsymbol{\sigma} : \boldsymbol{L}^* \, \mathrm{d}V - \int_{S_{\text{T}}} \boldsymbol{T}^{\text{sp}} \cdot \boldsymbol{v}^* \, \mathrm{d}S + \int_{S_+} \boldsymbol{T} \cdot (\boldsymbol{v}_-^* - \boldsymbol{v}_+^*) \, \mathrm{d}S = 0, \qquad (18)$$

where $\boldsymbol{u}$ and $\boldsymbol{v}$ are the displacement and velocity fields respectively, $\boldsymbol{v}_+$ and $\boldsymbol{v}_-$ are the respective velocities on the sides S_+ and S_- of the separating interface, the superscript $*$ denotes a kinematically admissible virtual quantity, $\boldsymbol{L}$ is the velocity gradient, $\boldsymbol{\sigma}$ denotes the Cauchy stress, and $\boldsymbol{A} : \boldsymbol{B} = A_{ij} B_{ij}$ for second order tensors $\boldsymbol{A}$ and $\boldsymbol{B}$. It is tacitly assumed in equation (18) that the side S_+ is not far apart from S_-. Given the solution for the displacements $\boldsymbol{u}_n$ at time t_n, the finite element scheme is marched in time by computing displacement increments $\Delta \boldsymbol{u}$ so that the solution $\boldsymbol{u}_{n+1} = \boldsymbol{u}_n + \Delta \boldsymbol{u}$ satisfies equation (18) at time $t_{n+1} = t_n + \Delta t$. Within this updated Lagrangian formulation scheme in which the interfacial coordinates are updated as straining proceeds, the loading steps are taken sufficiently small so as to ensure that the separation process at the interface is simulated in a way that no jumps are made from the ascending part of the traction–separation curve directly to the descending part (figure 3).

The Newton iteration method was employed to solve the finite element equations derived from equation (18) and each iteration involved the solution of the linearized equations $G(\Delta \boldsymbol{u}, \boldsymbol{v}^*) + \mathrm{d}G(\Delta \boldsymbol{u}, \boldsymbol{v}^*) = 0$ about the known solution $\boldsymbol{u}_n$ at time t_n for the correction $\mathrm{d}\Delta \boldsymbol{u}$ to the displacement increment $\Delta \boldsymbol{u}$. The Jacobian of the Newton iteration scheme[2] was calculated by differentiating equation (18)

$$\mathrm{d}G = \int_V \boldsymbol{L}^* : (\mathrm{d}\boldsymbol{\sigma} - \boldsymbol{\sigma} \, \mathrm{d}l^{\text{T}} + \mathrm{d}l_{kk} \boldsymbol{\sigma}) \, \mathrm{d}V + \int_{S_+} \frac{1}{J_{\text{s}}} \mathrm{d}\boldsymbol{T}^0 \cdot (\boldsymbol{v}_+^* - \boldsymbol{v}_-^*) \, \mathrm{d}S$$
$$- \int_{S_+} \left\{ \frac{1}{J_{\text{s}}} (\mathrm{d}l_{\text{pp}} - \mathrm{d}l_{\text{p}k} n_{\text{p}} n_k) + \mathrm{d}\left(\frac{1}{J_{\text{s}}}\right) \right\} \boldsymbol{T}^0 \cdot (\boldsymbol{v}_+^* + \boldsymbol{v}_-^*) \, \mathrm{d}S, \qquad (19)$$

where $\boldsymbol{l} = \partial(\Delta \boldsymbol{u})/\partial \boldsymbol{x}$, $\boldsymbol{x}$ refers to the position of a material point in the current configuration, $J_{\text{s}} = \mathrm{d}S/\mathrm{d}S_0$ is the ratio of the current to the reference area element, and $\boldsymbol{v} = \Delta \boldsymbol{u}/\Delta t$ is the velocity of a material point. The formulation of Govidarajan and Aravas (1994) was adopted to ensure zero lattice strain during large rigid body rotations and the incompressibility of the plastic deformation was enforced by the method of Nagtegaal *et al* (1974).

Following Sofronis and McMeeking (1989), one can cast equation (4) governing hydrogen transport through bulk material in the presence of transport through an internally decohering interface (cf equation (5)) into the weak statement

$$\int_V \frac{D}{D_{\text{eff}}} \dot{C}_{\text{L}} C_{\text{L}}^* \, \mathrm{d}V + \int_V \alpha \theta_{\text{T}} \frac{\mathrm{d}N_{\text{T}}}{\mathrm{d}\varepsilon^{\text{p}}} \dot{\varepsilon}^{\text{p}} C_{\text{L}}^* - \int_V \frac{DC_{\text{L}} V_{\text{H}}}{3RT} \nabla \sigma_{kk} \cdot \nabla C_{\text{L}}^* \, \mathrm{d}V$$
$$+ \int_V D \nabla C_{\text{L}} \cdot \nabla C_{\text{L}}^* \, \mathrm{d}V + \int_{S_{\text{N}}} \phi C_{\text{L}}^* \, \mathrm{d}s + \int_{S_+} \phi_+ C_{\text{L}}^* \, \mathrm{d}s + \int_{S_-} \phi_- C_{\text{L}}^* \, \mathrm{d}s = 0, \qquad (20)$$

---

[2] The authors are thankful to Professor N Aravas for many extensive discussions on the subject.

where S_N is the part of the outer boundary of the cell where the flux ϕ is prescribed, C_L^* is a virtual hydrogen concentration such that $C_L^* = 0$ on the part of the outer boundary S where C_L is prescribed, and ϕ_+ and ϕ_- are fluxes through the sides S_+ and S_-, respectively of the decohering interface away from the bulk material and into the interfacial channel. Similarly, the weak statement of equation (5) is stated as

$$\int_{S_+} \frac{\mathrm{d}}{\mathrm{d}t}[(C_L + C_T)u_n]C_L^* \,\mathrm{d}s + \int_{S_+} \frac{\mathrm{d}(\phi_{\text{int}}u_n)}{\mathrm{d}s}C_L^* \,\mathrm{d}s + \int_{S_-} \phi_-' C_L^* \,\mathrm{d}s + \int_{S_+} \phi_+' C_L^* \,\mathrm{d}s = 0 \qquad (21)$$

in which ϕ_+' and ϕ_-' are fluxes through the sides S_+ and S_-, respectively of the decohering interface away from the interfacial channel and into the bulk material (see figure 2). Integrating the second integral of equation (21) by parts and by combining equations (20) and (21) with $\phi_+' = -\phi_+$, $\phi_-' = -\phi_-$, one finds the weak statement for hydrogen transport through the bulk material containing an internal interfacial channel:

$$\int_V \frac{D}{D_{\text{eff}}}\dot{C}_L C_L^* \,\mathrm{d}V + \int_V \alpha\theta_T \frac{\mathrm{d}N_T}{\mathrm{d}\varepsilon^p}\dot{\varepsilon}^p C_L^* - \int_V \frac{DC_L V_H}{3RT}\nabla\sigma_{kk} \cdot \nabla C_L^* \,\mathrm{d}V$$

$$+ \int_V D\nabla C_L \cdot \nabla C_L^* \,\mathrm{d}V + \int_{S_N} \phi C_L^* \,\mathrm{d}S + \int_{S_+} \frac{\mathrm{d}}{\mathrm{d}t}[(C_L + C_T)u_n]C_L^* \,\mathrm{d}s$$

$$+ \int_{S_+} \left(D_{\text{int}}\frac{\mathrm{d}C_L}{\mathrm{d}s} - \frac{D_{\text{int}}V_H}{RT}C_L\frac{\mathrm{d}T_n}{\mathrm{d}s} \right)u_n \frac{\mathrm{d}C_L^*}{\mathrm{d}s}\,\mathrm{d}s + \phi_{\text{int}}u_n C_L^*\big|_{s=0}^{s=s_f} = 0, \qquad (22)$$

where $0 \leqslant s \leqslant s_f$ is arclength along the interface. If a zero flux or a constant concentration boundary condition is prescribed at the two ends ($s = 0$ and $s = s_f$) of the interface, then the last term on the right-hand side of equation (22) cancels out.

It is evident from equations (18) and (22) that the hydrogen transport initial/boundary-value problem and the elastoplastic boundary-value problem are fully coupled. The stress and deformation fields as furnished by the solution to equation (18) affect the calculation of the H concentration as furnished by equation (22), and in turn, the H concentration affects the calculation of the stress and deformation fields through its effect on the material constitutive law (equation (14)), flow stress (equation (8)), and interfacial cohesion (equations (15) and (17)). Therefore, the solution involves iteration and the finite element procedure details on the coupling of the solutions to equations (18) and (22) are stated in the work of Lufrano *et al* (1998b). It is emphasized again that in the updated Lagrangian formulation scheme employed in this work the interfacial tractions were calculated from equations (15) and (17) by using the interfacial concentration Γ_{n+1} (which varies with arclength at any instant of time) in the iterative scheme for the solution at time t_{n+1} of the coupled elastoplasticity equation (18) and hydrogen transport equation (22).

6. Numerical results

6.1. Finite element mesh and material constants

The first quadrant of the unit cell modelled is shown in figure 4. The radius of the cylindrical particle was $r/L = 0.25$, where $L = 2\,\mu$m was the size of the square cell. The applied macroscopic logarithmic strain is $\varepsilon_{22} = \ln(1 + U_2/L)$ and in response, the average applied macroscopic stress on the top face of the cell is σ_{22}, where U_2 is the uniform displacement in the two-direction of the top face. The unit cell was constrained to remain rectangular with zero average transverse stress and the end surfaces were required to remain planar during deformation. Both lateral and end surfaces were free of shear traction. By symmetry, the shear traction and the normal velocity are zero on $x_1 = 0$ and $x_2 = 0$. For both diffusion and
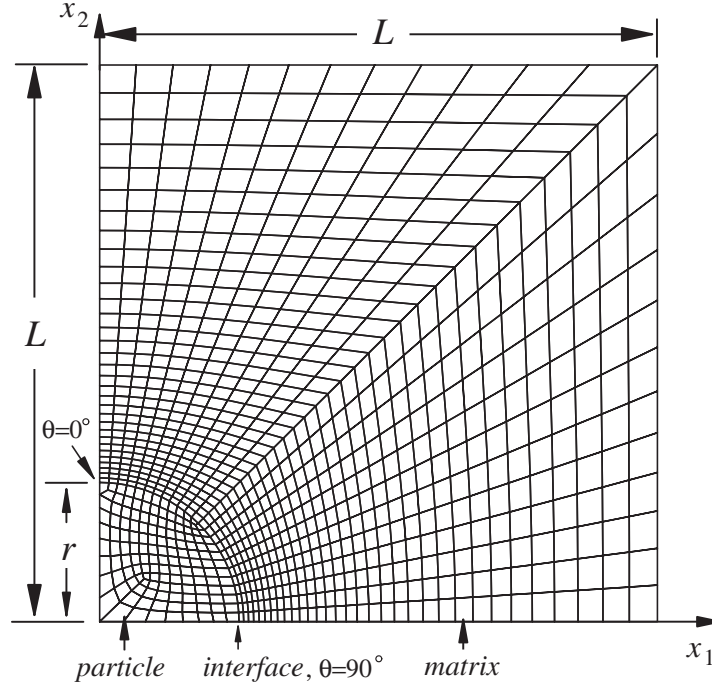
Figure 4. Finite element mesh and relevant dimensions of the first quadrant of the unit cell.

elastoplasticity problems the same finite element mesh was used consisting of a total of 908 four-node isoparametric elements with 986 nodes. The cylindrical particle was descritized by 140 four-noded isoparametric elements with 161 nodes. The matrix was descritized by 24 elements in the hoop direction and 32 elements in the radial direction. The element sides along the particle/matrix boundary were the sides of the interfacial cohesive elements. The matrix side was designated S_+ and the particle side S_- (figure 2). For the purpose of describing the location of a point along the interface the polar angle θ is used which is $0°$ where the interface cuts the x_2 axis ($s = 0$), and $90°$ where the interface cuts the x_1 axis ($s = s_f = \pi r/2$, see figure 4).

The cylindrical particle was linearly elastic and isotropic with Young's modulus $E_p = 270$ GPa and Poisson's ratio $\nu_p = 0.3$. The response of the matrix was elastoplastic: the elasticity was linear and isotropic with Young's modulus $E_m = 206.8$ GPa and Poisson's ratio $\nu_m = 0.3$. The plastic response was characterized by the flow stress in uniaxial tension shown in figure 5. The initial yield stress in the absence of hydrogen was $\sigma_0 = 220$ MPa. For the maximum cohesive strength in the absence of hydrogen, it was assumed that $\hat{\sigma}(0) = 3\sigma_0$, and hence $\delta_n = 9.95$ nm by equation

$$(2\gamma_{\text{int}})_0 = 2\gamma_s - \gamma_i = \delta_n \int_0^1 \sigma(q', 0)\, dq' = 9\hat{\sigma}(0)\frac{\delta_n}{16},$$

where the subscript 0 denotes absence of hydrogen, $\gamma_s = 2.280$ J m^{-2} is the surface energy and $\gamma_i = 0.866$ J m^{-2} is the interface energy taken equal to the grain boundary energy (Hirth and Lothe 1982). Further, it was assumed that $\delta_t = \delta_n$ for the tangential separation. It should be noted that Symons (1998), based on the work by Brown and Stobbs (1976) and Goods and Brown (1979), calculated an interfacial fracture stress in precipitation hardened alloy 690
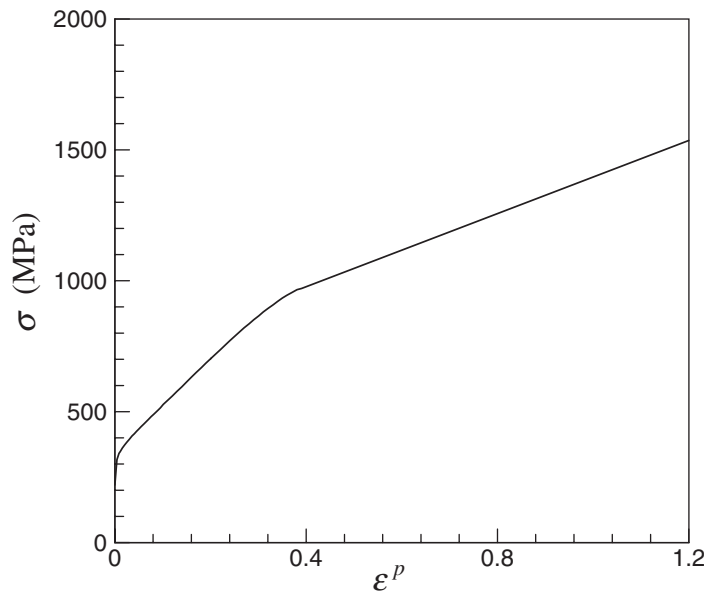
Figure 5. Plastic response of the matrix in the absence of hydrogen. The yield stress is $\sigma_0 = 220\,\text{MPa}$.

varying from about 600 to 1000 MPa depending on the heat treatment and hydrogen content. In this paper, the value of $3\sigma_0$ chosen for $\hat{\sigma}(0)$ is within the estimated limits.

Hydrogen diffused through the matrix, the particle, and along and across the particle/matrix interface. Zero flux boundary condition was enforced on the outer boundaries and the symmetry planes of the unit cell, i.e. $\phi = 0$ along $x_1 = 0, L$ and $x_2 = 0, L$. Trapping in the deforming matrix was associated with dislocations. The binding energy of hydrogen at dislocations was taken equal to $W_B = 9.64\,\text{kJ mole}^{-1}$ (Thomas 1989). Assuming one trap per atomic plane threaded by a dislocation, one finds that the trap density in traps per cubic metre is given by $N_T = \sqrt{2}\rho/a$, ρ is the dislocation density assumed to increase linearly with plastic deformation (Gilman 1969), that is, $\rho = \rho_0 + \gamma\varepsilon^p$ for $\varepsilon^p < 0.5$ and $\rho = \text{const.}$ for $\varepsilon^p \geqslant 0.5$, $\rho_0 = 10^{10}$ line length (m) per cubic metre, and $\gamma = 2.0 \times 10^{16}$ line length m^{-3}. No trapping of hydrogen was considered inside the elastically deforming cylindrical particle. According to the discussion in section 4, interfacial trapping along the particle/matrix interface was modelled by the introduction of a volumetric trap density within the volume of the opening interface that was constant during deformation and equal to $N_T = 2/\alpha a^2 \delta_n$. Considering one trapping site per trap ($\alpha = 1$) and $\delta_n = 9.95\,\text{nm}$, one calculates $N_T = 1.569 \times 10^{27}$ atoms m^{-3}. The trapping energy of the interface was $W_B = -\Delta h_i = 26.0\,\text{kJ mole}^{-1}$ (Young and Scully 1997). The molar volumes of the matrix, the particle, and the interface were taken equal to $V_M = 6.98\,\text{cm}^3\,\text{mole}^{-1}$. Similarly, the corresponding partial molar volumes of hydrogen were also assumed equal to $V_H = 1.72\,\text{cm}^3\,\text{mole}^{-1}$ (Baranowski *et al* (1971) for the partial volume in the matrix) and hence, $\lambda = 0.2464$. The system's temperature was $T = 300\,\text{K}$.

The diffusion constants through NILS for the particle and the matrix were assumed to be the same, $D = 1.0209 \times 10^{-15}\,\text{m}^2\,\text{s}^{-1}$ (Enmgelmann *et al* 1995). The hydrogen diffusion constant along the particle/matrix interface was assumed to be $D_\text{int} = kD$, where k is a multiplier, in view of the absence of any experimental results on the subject. However, it is well known that for the case of hydrogen diffusion through grain boundaries in nickel, the
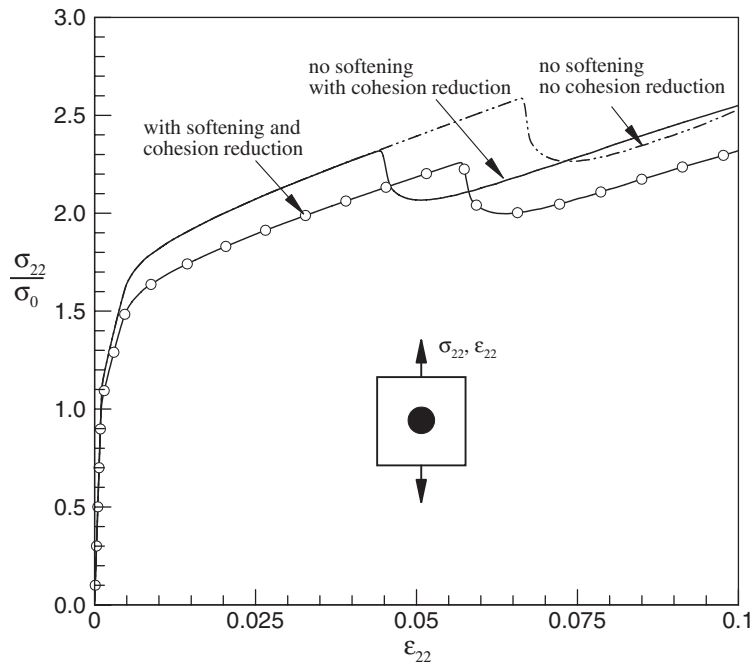
Figure 6. Normalized average true stress σ_{22}/σ_0 versus macroscopic logarithmic strain ε_{22} at a macroscopic strain rate $4.0 \times 10^{-4}\,\mathrm{s}^{-1}$. For the case with hydrogen-induced softening, $\xi = -49$.

diffusion coefficient is a multiple of that in the matrix and the multiplier has been assessed to vary between 1 and 100 (Yao and Cahoon 1988).

6.2. Absence of hydrogen-induced matrix softening

6.2.1. Interfacial decohesion. Two series of calculations were carried out: one in which the interfacial cohesion was not affected by the presence of hydrogen (equations (15) and (17) with $\Gamma = 0$ so that $\hat{\sigma}(\Gamma) = \hat{\sigma}(0)$), and one in which the hydrogen effect on cohesion was accounted for (equations (15) and (17) with $\Gamma \neq 0$). In both series, hydrogen was residing and diffusing through the matrix, the particle, and the interface, and was assumed to have no effect on the flow characteristics of the matrix (equations (8) and (9) with $\xi = 1$). The hydrogen diffusion through the interfacial channel was $D_{\mathrm{int}} = 5D$. The initial hydrogen concentration was $C_L^0 = 1.518 \times 10^{26}\,\mathrm{H\,atoms\,m}^{-3}$ (30 wppm) and the loading rate $\mathrm{d}U_2/\mathrm{d}t$ was constant and equal to $0.0008\,\mu\mathrm{m\,s}^{-1}$ which at time $t = 0$ corresponds to the strain rate of $4 \times 10^{-4}\,\mathrm{s}^{-1}$ used by Symons (1998) in his investigation of alloy 690.

The normalized average macroscopic stress σ_{22}/σ_0 in the unit cell is plotted in figure 6 against the macroscopic logarithmic strain $\varepsilon_{22} = \ln(1+U_2/L)$. The stress rises at the beginning, then drops abruptly to a certain level, and then rises again. The drop in stress indicates that decohesion is taking place. The drop occurs at $\varepsilon_{22} = 0.0443$ and $\sigma_{22}/\sigma_0 = 2.31$ when hydrogen affects interfacial cohesion, and at $\varepsilon_{22} = 0.0663$ and $\sigma_{22}/\sigma_0 = 2.59$ in the absence of the hydrogen effect on cohesion. It is interesting to note that before decohesion begins to have an effect on the stress–strain curve (i.e. for $\varepsilon_{22} \leqslant 0.0443$), the two curves coincide.

The normal, $T_n^0/3\sigma_0$, and tangential, $T_t^0/3\sigma_0$, nominal tractions on the interface are plotted in figures 7(*a*) and (*b*) as functions of the angle θ along the interface (see inset of figure 7(*a*)).
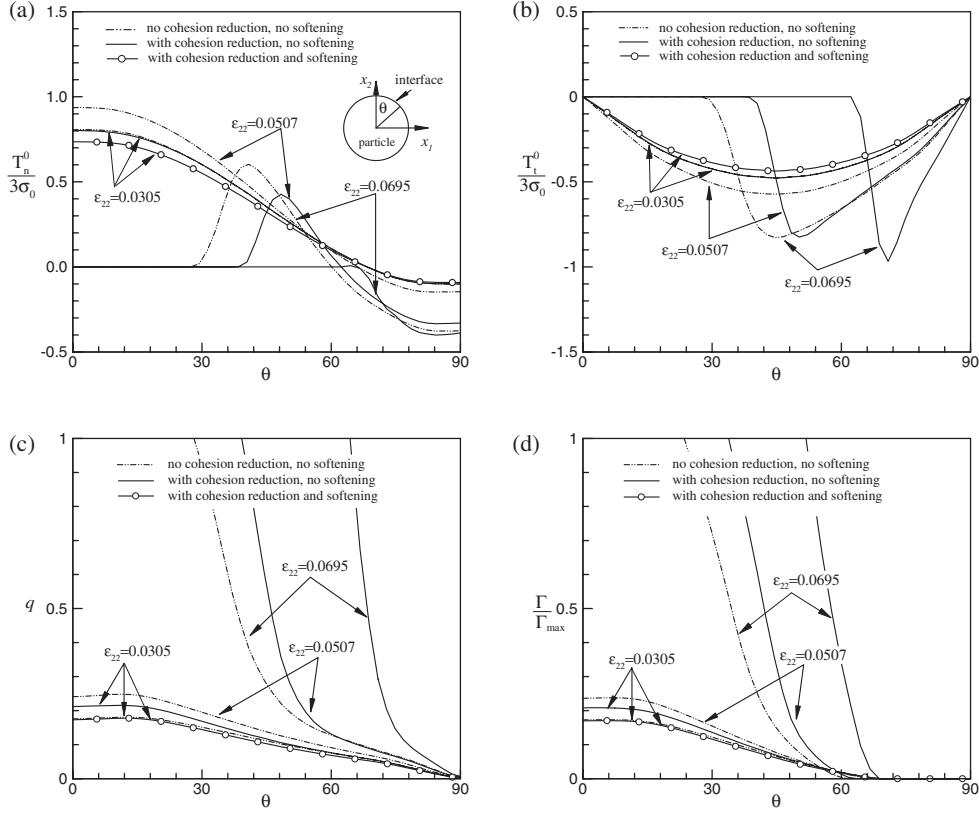
Figure 7. Interfacial profiles of (*a*) the normalized normal traction $T_n^0/3\sigma_0$; (*b*) the normalized tangential traction $T_t^0/3\sigma_0$; (*c*) the separation parameter q; and (*d*) the normalized interfacial hydrogen coverage Γ/Γ_{max}. Profiles for macroscopic strains $\varepsilon_{22} = 0.0507$ and 0.0695 are in the absence of softening. For $\varepsilon_{22} = 0.0305$, the profiles for hydrogen-induced softening ($\xi = -49$) are also superposed. The macroscopic strain rate was equal to 4.0×10^{-4} s^{-1}.

At macroscopic strain $\varepsilon_{22} = 0.0305$, i.e. before interfacial decohesion begins to affect the deformation of the cell significantly, the normal traction is positive close to the top of the particle ($\theta = 0°$) and decreases to negative values close to the side of the particle at $\theta = 90°$. Due to the straining in the x_2-direction, the part of the interface close to the top of the particle opens up, thus experiencing a closing tensile traction, whereas the part close to the side of the particle is under compression due to the matrix plastic flow in the negative x_2-direction against the particle that behaves almost as rigid inclusion. At the same macroscopic strain $\varepsilon_{22} = 0.0305$, the tangential nominal traction T_t^0 is non-positive with $T_t^0 = 0$ at $\theta = 0°$ and $90°$ and attains its maximum magnitude at $\theta \approx 45°$ (figure 7(*b*)). Thus, traction T_t^0 on S_+ (figure 2) points toward the direction of increasing θ away from the top of the particle. The fact that both normal and tangential interfacial tractions (figures 7(*a*) and (*b*)) are the same for the hydrogen-affected and non-affected cohesion at a typical strain (e.g. $\varepsilon_{22} = 0.0305$) prior to the strain $\varepsilon_{22} = 0.0443$ at which the decohesion effect becomes significant is in agreement with the coincidence shown in figure 6 between the corresponding macroscopic stress–strain curves. Figure 7(*c*) shows that at strain $\varepsilon_{22} = 0.0305$ the separation parameter q attains its maximum at $\theta \approx 15°$ for both cases of hydrogen-affected and non-affected interfacial cohesion. In addition, separation q is larger for the hydrogen-affected interface than the non-affected interface. This

means that separation in the former case takes place at less load than in the latter (figure 6). With regard to the debonding initiation site, figure 7(c) shows that debonding does not initiate at the top of the particle (axis of symmetry), but rather at the oblique direction of $\theta \approx 15°$. As the macroscopic load increases and the separation parameter reaches $q = \frac{1}{3}$ at $\theta \approx 15°$, the debonding propagates very rapidly toward the symmetry axis, and a part of completely decohered interfacial segment appears to be the case over the sector $0 \leqslant \theta \leqslant \theta_0$, where θ_0 increases with increasing macroscopic strain (figure 7(c)) and is larger when the hydrogen effect on the interface cohesion is accounted for (figure 7(c)). Along this segment, both normal and tangential tractions are zero (figures 7(a) and (b)). As a result, there is an intensification of the interfacial tractions over the part $\theta_0 \leqslant \theta \leqslant 90°$ of the interface as a fraction of the macroscopically applied load is transferred there. As can be seen from figure 7(a), at strain $\varepsilon_{22} = 0.0695$ the normal traction is negative over almost the entire undebonded sector when the hydrogen effect on the interfacial cohesion is accounted for. In other words, the interface ahead of the crack tip experiences compression and this makes it harder for the debond length to advance further.

In figure 7(d) the interfacial hydrogen concentration is plotted as the two sides separate. When hydrogen affects the cohesion, the interfacial coverage is greater than when hydrogen does not affect the cohesion in agreement with figure 7(c) which indicates that the separation increases when the hydrogen effect on cohesion is present. Once separation takes place and the interface sides become independent free sides loaded with zero traction, the definition of interfacial coverage Γ in terms of C_T as discussed in section 4 becomes meaningless and this is the reason why no $\Gamma/\Gamma_{\max}$ is reported in figure 7(d) over the completely debonded part of the interface. Also the interfacial coverage is zero over about $60° \leqslant \theta \leqslant 90°$, and this reflects the fact that the interface is under compression (figure 7(a)) and the normal separation is zero despite the fact that the total separation (which is purely tangential) shown in figure 7(c) is non-zero.

In figure 8 the total normalized strain energy E_{tot}/E_0 absorbed by the cell and the energy expended at the interface E_{int}/E_0 during deformation are plotted against the macroscopic logarithmic strain ε_{22}. The total energy absorbed, E_{tot}, was calculated through $E_{\text{tot}} = \int F_2 \, dU_2$, where F_2 is the total force on the boundary $x_2 = L$ of the unit cell (see figure 4). The energy consumed over interfacial separation was calculated through

$$E_{\text{int}} = \iint (T_n^0 \, dS^0 \, du_n + T_t^0 \, dS^0 \, du_t).$$

The non-dimensionalizing energy is $E_0 = A_0(2\gamma_{\text{int}})_0$, where A_0 is the original undeformed area of the inclusion/matrix interface. One can clearly see that for both cases of hydrogen-affected and unaffected decohesion, the total energy absorbed by the specimen is almost the same up to strain $\varepsilon_{22} = 0.0443$ at which no substantial interface debonding is present to affect the overall macroscopic deformation of the cell. When $\varepsilon_{22} > 0.0443$, the total energy absorbed in the case of hydrogen-affected decohesion is less than that when the hydrogen decohesion effect is absent, and this is a direct result of the fact that the macroscopic axial stress σ_{22} is relaxed after the interface begins to decohere (figure 6). On the other hand, the energy absorbed at the interface for hydrogen-affected decohesion is greater than that for hydrogen unaffected up to $\varepsilon_{22} \approx 0.089$ (figure 8). This derives from the fact that when hydrogen affects the interfacial cohesion it softens the interface, thereby allowing for larger separations as shown in figure 7(c) than those when the effect on cohesion is absent. However, at large macroscopic strains (e.g. $\varepsilon_{22} > 0.089$), the interfacial undebonded length is almost the same for both hydrogen-affected and hydrogen unaffected interface. Since hydrogen reduces the reversible work of separation per unit area, one deduces that the work of separation E_{int} in the former case is smaller than that in the latter (see figure 8). Also, it is worth noting that the energy expended on interfacial
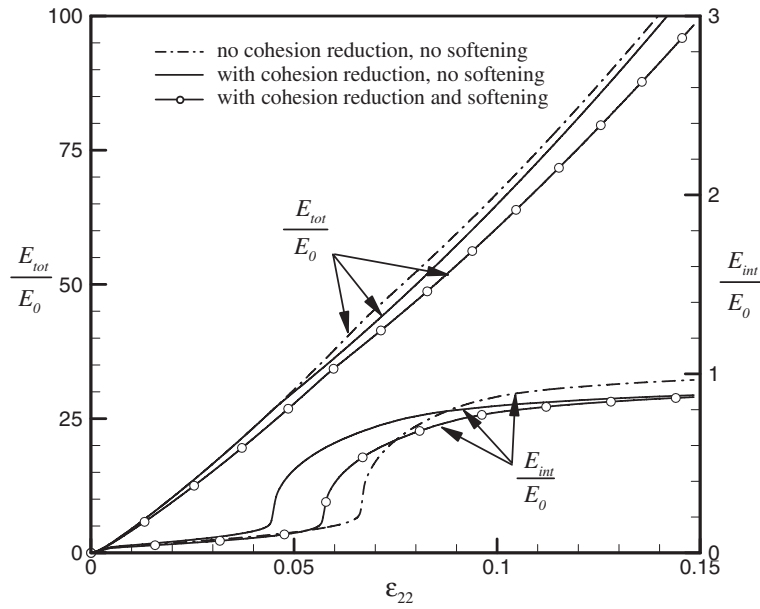
Figure 8. Plot of the normalized total energy E_{tot}/E_0 absorbed by the unit cell and normalized energy E_{int}/E_0 absorbed by the interface against the macroscopic logarithmic strain ε_{22} at a macroscopic strain rate $4.0 \times 10^{-4}\,\mathrm{s}^{-1}$, where $E_0 = (2\gamma_{int})_0 A_0$, with A_0 being the initial undeformed area of the interface.

decohesion is only a very small fraction of the total energy, which indicates that it is the bulk plasticity that governs the energetics of the process.

6.2.2. Hydrogen transport during interfacial decohesion. In this subsection, the hydrogen transport is discussed in relation to the two series of simulations reported, namely in the absence of any softening effect.

Figure 9 shows the distribution of normalized total hydrogen concentration $(C_L + C_T)/C_L^0$ in the specimen at three different stages of loading when hydrogen does not affect the cohesive strength (left column) and when hydrogen affects the cohesive strength (right column). At the early stages of loading ($\varepsilon_{22} = 0.0305$), hydrogen accumulates in the high hydrostatic-stress zone at the top of the particle along the segment of the interface $10° < \theta < 30°$ (around point A in figures 9(a) and (a′)). On the other hand, the zone with the lowest hydrostatic stress over the sector $60° < \theta < 80°$ (around point B in figures 9(a) and (a′)) is depleted. Obviously, due to the slow loading rate long-circuit diffusion drives the hydrogen from regions of low hydrostatic stress to those of high hydrostatic stress. At point A, hydrogen by decreasing locally the interfacial cohesive strength assists in the formation of the first complete decohesion site which rapidly propagates toward the top of the particle ($\theta = 0°$) resulting in an interfacial debond segment once the macroscopic straining gets greater than $\varepsilon_{22} \approx 0.0663$ for the hydrogen unaffected cohesion case (figure 9(b)) and $\varepsilon_{22} = 0.0443$ for that with the cohesion effect accounted for (figure 9(b′)).

Since the interfacial tractions on the debonded section of the interface reduce to zero, the hydrostatic stress in the matrix and the particle on the sides of the debonded interfacial segment also decreases. This reduces locally the influence of the hydrostatic stress on setting the chemical potential gradients responsible for hydrogen diffusion through the matrix and
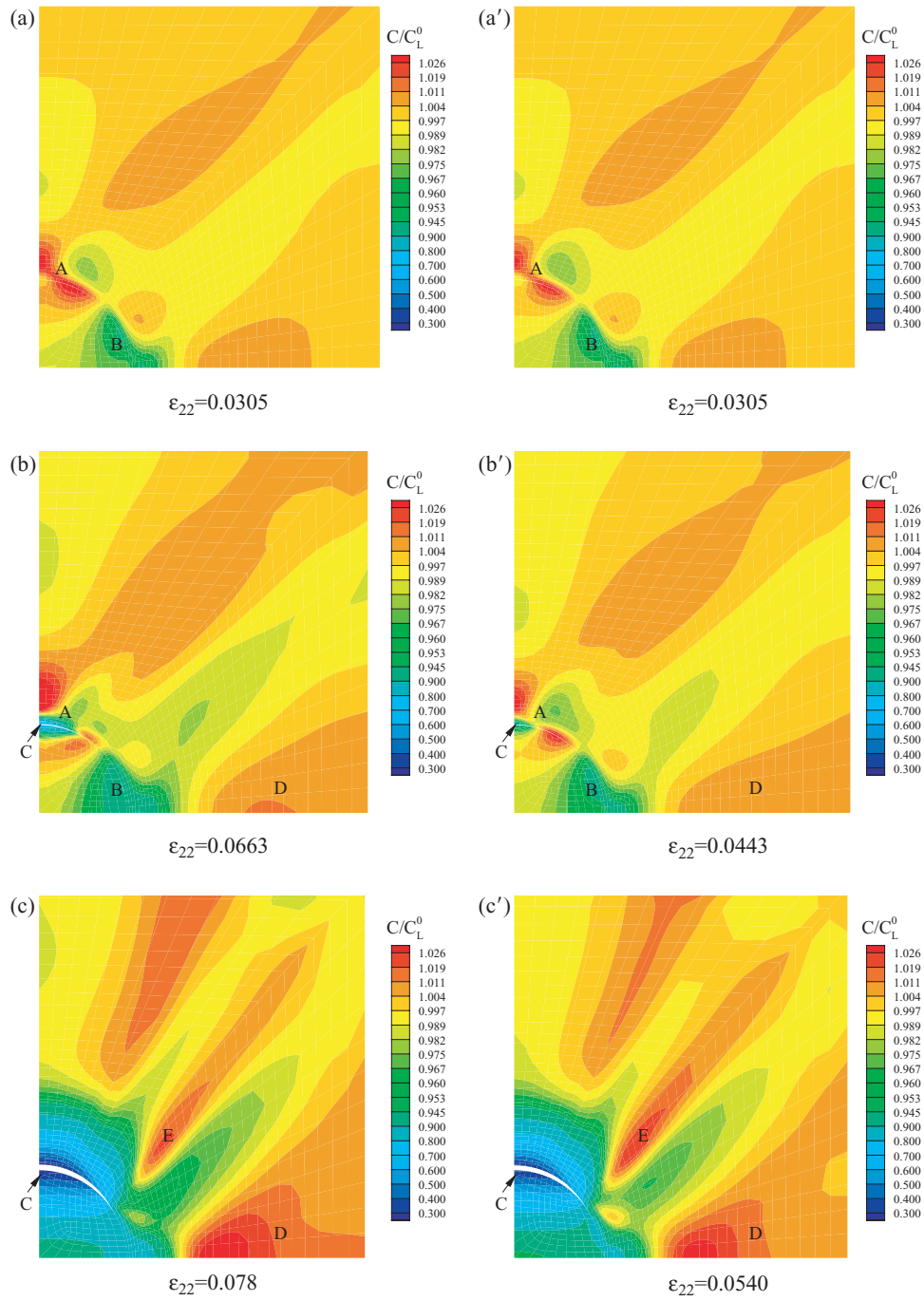
Figure 9. Contours of normalized hydrogen concentration C/C_L^0 as the load increases in the absence of hydrogen-induced matrix softening. The left column is for the case when hydrogen does not affect the interfacial cohesion and the right column is when hydrogen affects the interfacial cohesion. The macroscopic strain rate in both cases was $4.0 \times 10^{-4}\,\mathrm{s}^{-1}$.

the particle. Also the opened interface with its enhanced volume constitutes a sink for the hydrogen solutes that draws hydrogen away from the entire surrounding region. Thus, the chemical potential gradients are now dominated by the local concentration gradients set by the formation of the open interfacial channel. As a result, the opened interfacial channel is embedded in a hydrogen-depleted zone when the decohesion begins (area around point C in figures 9(b) and (b′)) and at a later stage when the interfacial debond length spans the angle $0 \leqslant \theta \leqslant 45°$ (area around point C in figures 9(c) and (c′)). The enhanced hydrogen concentration observed at the area centred at point E in figures 9(c) and (c′) is associated with the local rising of the hydrostatic stress due to the formation of the interfacial channel.

With a sufficiently large debonded interfacial length (e.g. as in figures 9(c) and (c′)), the applied macroscopic load is sustained primarily by the matrix ligament between the particles, which results in the development of a local stress concentration in the ligament. As the interface continues to decohere with increasing load and the hydrostatic stress in the ligament between adjacent inclusions continues to rise, hydrogen accumulates in the space between the inclusions (site D in figures 9(c) and (c′)). This is the case in which hydrogen can trigger decohesion along a grain boundary in the ligament between the particles, thus leading to failure through propagation of a macrocrack along grain boundaries decorated by carbide particles.

6.3. Hydrogen-affected interfacial decohesion in the presence of hydrogen-induced matrix softening

In this section, the hydrogen-induced softening as described by equations (8), (9), and (14) was accounted for in the analysis of the deformation of the unit cell while equations (15) and (17) were used to describe the hydrogen effect on interfacial cohesion. The initial NILS hydrogen concentration was $C_L^0 = 1.518 \times 10^{26}$ atoms m^{-3} (30 wppm), the diffusion coefficient through the interfacial channel was $D_{int} = 5D$, and the loading rate dU_2/dt was constant and equal to $0.0008 \, \mu m \, s^{-1}$ as before in the absence of softening. The softening parameter ξ in equation (9) was set equal to -49.0. Thus, at time $t = 0$ (with $C_L^0 = 1.518 \times 10^{26}$ atoms m^{-3} and $V_M = 6.98 \, cm^3 \, mole^{-1}$) the initial yield stress of the matrix was 91.2% of the yield stress σ_0 in the absence of hydrogen.

The normalized macroscopic true stress σ_{22}/σ_0 as a function of the macroscopic logarithmic strain and the interfacial parameters (T_n^0, T_t^0, q, and Γ/Γ_{max}) as functions of arclength along the interface are shown superposed in figures 6 and 7, respectively, along with the other curves (interfacial cohesion affected and unaffected) in the absence of softening. It is clear that with hydrogen-induced softening, the macroscopic strain at which decohesion initiates is larger than that in the absence of the softening effect (figure 6). In the former case, macroscopic stress relaxation due to hydrogen-induced decohesion takes place at strain $\varepsilon_{22} = 0.0570$ whereas in the latter at $\varepsilon_{22} = 0.0443$. Also in the case of hydrogen-induced matrix softening, the maximum macroscopic stress at the onset of the decohesion-related relaxation ($\sigma_{22}/\sigma_0 = 2.25$) is slightly smaller than that in the case of no softening ($\sigma_{22}/\sigma_0 = 2.31$). Evidently hydrogen-induced softening relaxes the stress in the matrix and the particle, and this results in milder tractions sustained at the interface in comparison to those in the absence of the softening effect. Thus normal interfacial traction reduction due to softening at the early stages of decohesion leads to milder hydrogen concentration built-up at the interface (figure 7(d)) and as a result, the interface experiences a weaker hydrogen effect on its cohesive strength. As a consequence, a higher macroscopic strain is needed for the traction required for interfacial decohesion to develop when the softening effect is present than that needed when the softening effect is absent. Indeed, figures 7(a) and (b) show that before the macroscopic stress relaxation takes place (e.g. $\varepsilon_{22} = 0.0305$), the magnitudes of the normal

and tangent tractions on the interface for the case of hydrogen-induced softening are slightly less than those for the case without the softening effect. The interfacial separation parameter q and the interfacial coverage (figures 7(c) and (d)) exhibit similar response.

The graphs of the total normalized strain energy E_{tot}/E_0 absorbed by the cell and the energy E_{int}/E_0 expended at the interface against macroscopic logarithmic strain ε_{22} are shown superposed in figure 8 along with the corresponding graphs in the absence of the softening effect. Clearly, the larger macroscopic stress relaxation associated with the softening effect (figure 6) results in a smaller energy E_{tot} absorption by the unit cell. Further, at large macroscopic strains (e.g. $\varepsilon_{22} \geqslant 0.09$) when the interfacial debond segment is approximately the same for all cases considered, softening causes the energy expended on interfacial decohesion E_{int}/E_0 to be slightly less than that in the absence of softening. Probably, this is a result of softening-induced reduction of the interfacial tractions.

In summary, the softening effect delays the interfacial decohesion in the sense that larger macroscopic strains are sustained by the material before the onset of decohesion. On the other hand, the softening effect reduces the maximum stress for the onset of decohesion and the energy absorbed by the matrix and the interface. Thus, one may argue that hydrogen-induced softening embrittles both the overall unit cell and interfacial responses.

6.4. Strain rate effect

The effect of strain rate on decohesion was investigated by loading the unit cell at macroscopic strain rates $\dot{\varepsilon}_{22} = 0.4\,\text{s}^{-1}$ ($dU_2/dt = 0.8\,\mu\text{m s}^{-1}$) and $\dot{\varepsilon}_{22} = 4.0\,\text{s}^{-1}$ ($dU_2/dt = 8\,\mu\text{m s}^{-1}$) that were higher than the rate $\dot{\varepsilon}_{22} = 4.0 \times 10^{-4}\,\text{s}^{-1}$ ($dU_2/dt = 0.0008\,\mu\text{m s}^{-1}$) at which all calculations reported so far were carried out. The initial NILS hydrogen concentration C_L^0 was equal to $1.518 \times 10^{26}\,\text{atoms m}^{-3}$ and the interface diffusion constant was five times as large as that of the matrix. The hydrogen effect on interfacial cohesion was accounted for as described by equations (15) and (17). No hydrogen-induced softening in the matrix was considered ($\xi = 1.0$).

Figure 10(a) shows that as the macroscopic strain rate increases, both the applied stress and strain at which relaxation due to decohesion occurs increase. The normalized macroscopic nucleation stress σ_{22}/σ_0 is equal to 2.31, 2.38, and 2.45, respectively for applied macroscopic strain rate equal to 0.0004, 0.4, 4.0 s^{-1} and the corresponding strains are 0.0443, 0.0493, and 0.0546. Notably, there is no hydrogen or strain rate effect on the macroscopic stress–strain curve prior to this relaxation. As before, figure 10(b) shows that the hydrogen reduces the energy expended on interfacial decohesion for the same debond length (i.e. $\varepsilon_{22} \geqslant 0.09$) and at all applied strain rates. In particular, this energy increases and approaches that expended in the absence of the hydrogen effect as the strain rate increases. Figure 10(c) indicates that decohesion initiates at about $\theta \approx 15°$ as before regardless of the strain rate and the interfacial separation reduces as the strain rate increases. This is in agreement with figure 10(d) which shows that the interfacial concentration decreases with strain rate which makes the interface stronger. It is interesting that at the extremely high strain rate of 4.0 s^{-1}, there is a trough in the interfacial hydrogen-coverage profile at $\theta \approx 6°$ with two associated peaks at $\theta = 0°$ and $\theta \approx 15°$.

The distribution of the hydrogen concentration in the unit cell under applied macroscopic strain rate $\dot{\varepsilon}_{22} = 4.0\,\text{s}^{-1}$ is shown in figure 11. Due to the extremely short time available for hydrogen diffusion, the demand for hydrogen by the opening interface results in marked hydrogen population reduction in the zone immediately adjacent to the opening sides. During the initial debonding event ($\varepsilon_{22} = 0.0305$) and after extensive debonding has taken place ($\varepsilon_{22} = 0.0695$), two very narrow zones adjacent and parallel to the debond length are depleted
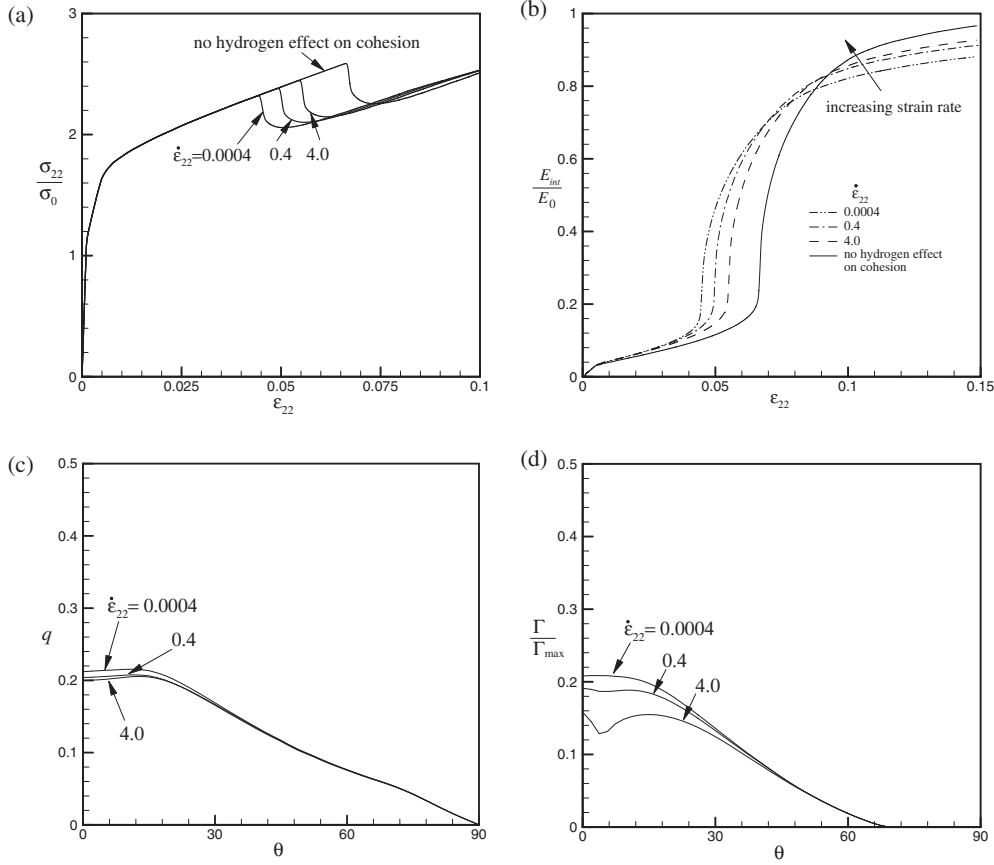
Figure 10. Strain rate effect on (*a*) the stress–strain curve of the unit cell; (*b*) the energy absorption at the interface; (*c*) interfacial separation parameter q; (*d*) interfacial hydrogen coverage Γ/Γ_{max} at macroscopic strain $\varepsilon_{22} = 0.0305$. No softening effect was considered.

of hydrogen by as much as 70%. Such a hydrogen reduction sets concentration gradients in the direction normal to the interface which though, owing to the short time available for diffusion, are not capable of maintaining a gradual monotonic variation of the hydrogen field as one moves in a direction normal to the interfacial side. Thus, the hydrogen spatial distribution is characterized by alternating zones of high and low hydrogen concentration parallel to the opening interface. In the region far away from the interface, the concentration of hydrogen is uniform and equal to the initial concentration. In general, it can be said that during very fast straining, there is no time for long-circuit diffusion to transport hydrogen from regions afield, and as result the hydrogen distribution is dominated by short (local) circuit effects. Last it should be mentioned that when the hydrogen-induced softening effect was accounted for in the calculations, the numerical results were not very different qualitatively and quantitatively from the ones reported in the absence of the softening effect.

6.5. *Effect of interfacial diffusivity*

In all previous calculations, the hydrogen diffusion constant along the interface was taken to be $D_{int} = 5D$, which is a value that is likely to be realistic. However, in the absence
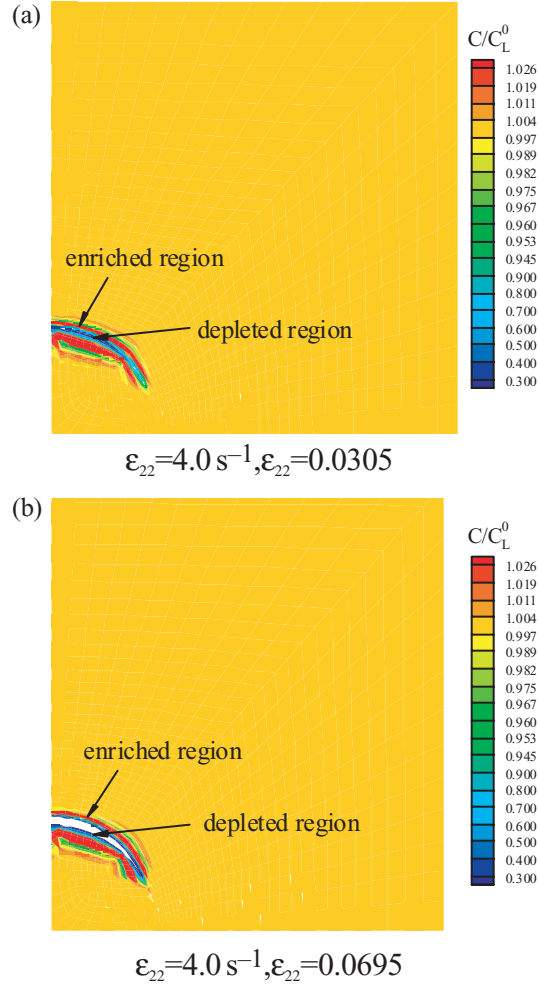
(a)

$\dot{\varepsilon}_{22}=4.0\,\mathrm{s}^{-1}, \varepsilon_{22}=0.0305$

(b)

$\dot{\varepsilon}_{22}=4.0\,\mathrm{s}^{-1}, \varepsilon_{22}=0.0695$

Figure 11. Contours of normalized hydrogen concentration C/C_L^0 in the specimen. The macroscopic strain rate was $4.0\,\mathrm{s}^{-1}$. The hydrogen effect on interfacial cohesion was accounted for and no softening was considered.

of any conclusive evidence on the magnitude of D_{int}, additional simulations with interfacial diffusion constant $D_{\mathrm{int}} = 100D$ were carried out to assess the importance of diffusion through the opening interfacial channel on interfacial decohesion. In the calculations, hydrogen was assumed to affect the interfacial properties as stated by equations (15) and (17), and no matrix softening was accounted for. All other material and loading parameters were the same as those reported in section 6.2.

Figure 12 shows the distribution of hydrogen in the cell before and after decohesion. By comparing figure 9(a') ($D_{\mathrm{int}} = 5D$) with figure 12(a) ($D_{\mathrm{int}} = 100D$), one sees that at the early stages of loading prior to interfacial decohesion and under the same macroscopic strain rate ($0.0004\,\mathrm{s}^{-1}$) and macroscopic strain $\varepsilon_{22} = 0.0305$, hydrogen accumulates at the high-hydrostatic stress area close to the particle top at larger amounts when the interfacial diffusion coefficient is larger. Correspondingly, larger regions are depleted around the low hydrostatic-stress region. Shortly after partial debonding takes place along the interface (cf figures 11(b) and 8(c')), one does not see any dramatic dependence of the hydrogen populations around the
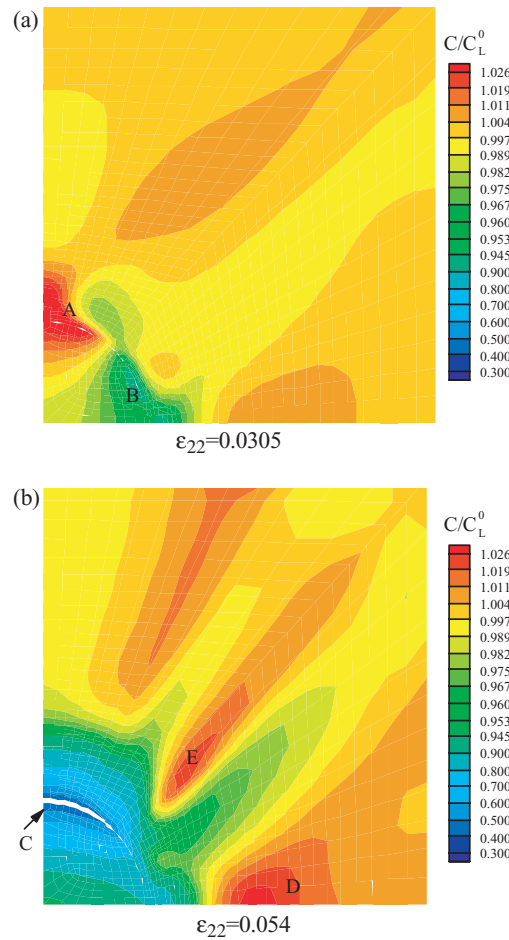
Figure 12. Contours of normalized hydrogen concentration C/C_L^0 in the specimen. The macroscopic strain rate was $4 \times 10^{-4} \text{ s}^{-1}$ and the interfacial diffusivity $D_{int} = 100D$. The hydrogen effect on interfacial cohesion was accounted for and no softening was considered.

opened interfacial segment on the interfacial diffusivity. Since the remaining undebonded part of the interface is under compression and with concentration gradients driving the hydrogen toward $\theta = 90°$ (figure 7(d)), there is no interfacial diffusion mechanism for bringing hydrogen to the tip of the interfacial channel.

Thus, the numerical results indicate that the value of the interfacial diffusion constant while it affects the early-stage concentration development, it does not seem to affect the hydrogen populations during interfacial debonding.

7. Discussion

A first conclusion to be drawn from the calculation results is that the elevations of the hydrogen concentration during interfacial decohesion and matrix/particle deformation are small in comparison to C_L^0, of the order of 3%. Such elevations do not yield dramatic inhomogeneities in the local flow stress and a concomitant triggering of pronounced patterns of inhomogeneous
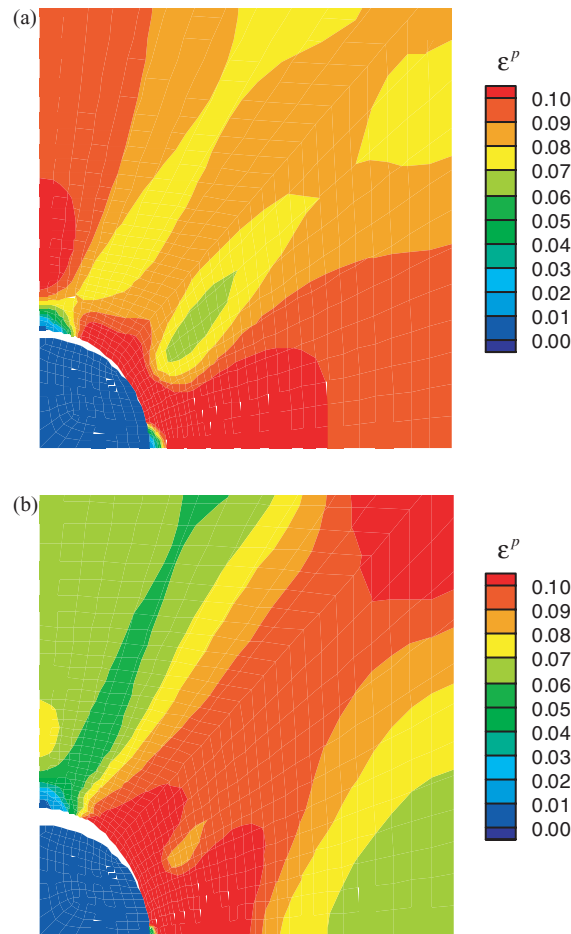
Figure 13. Contours of effective plastic strain ε^p at $\varepsilon_{22} = 0.078$ in the unit cell in the absence of hydrogen-induced softening: (a) without hydrogen effect on interfacial cohesion; (b) with hydrogen effect on interfacial cohesion. For both cases the macroscopic strain rate was $4 \times 10^{-4}\,\mathrm{s}^{-1}$ and $D_{\mathrm{int}} = 5D$.

plastic flow in the form of localized shear. In general, it was found that the yield stress was reduced by at most 10% in the areas of the highest hydrogen concentration. On the other hand, the calculations reveal a discernible loading rate effect on the transient hydrogen populations (figure 11) and the macroscopic stress–strain curve (figure 10(a)). This effect is in accord with suggestion that the dependence of the hydrogen embrittlement on the loading rate is associated with the ability of hydrogen diffusion to deliver sufficient amounts of hydrogen to the fracture initiation sites (Symons and Thompson 1997).

Another important conclusion is that the mechanisms of hydrogen-induced plasticity and hydrogen-induced decohesion should not be thought of as acting separately when assessing hydrogen embrittlement. If the mechanisms are operative, they act in concert. This is demonstrated by figure 13 in which the contours of the effective plastic strain ε^p are plotted for the case when hydrogen does not affect interfacial decohesion (figure 13(a)) and when hydrogen affects decohesion (figure 13(b)) at the same macroscopic logarithmic strain $\varepsilon_{22} = 0.078$ and in the absence of hydrogen-induced matrix softening. It is well known

that particle decohesion affects the plasticity in the deforming matrix. Needleman and Xu (1993) demonstrated that strong interface characteristics combined with low triaxiality allow for extensive plastic deformation prior to full interfacial debonding. The present numerical results of figure 13(b) clearly show that hydrogen by weakening the interfacial cohesion triggers plastic flow localization. On the other hand, when the interface is stronger due to the absence of the hydrogen effect (figure 13(a)) the plasticity is more diffuse. Hence, the widely held idea that decohesion and shear localization are phenomena mutually exclusive seems to be simplistic.

With regard to the uncertainty in the determination of the interfacial diffusion coefficient, the present finite element results show that the interfacial diffusivity affects the hydrogen concentration development along the interface before the onset of the initial debonding. However, the magnitudes of the macroscopic stress and strain at which the first debonding occurs are not dependent on the magnitude of the interface diffusion. This is attributed to the fact that, owing to the high interfacial trap binding energy (0.27 eV), the traps are saturated immediately upon loading, and thus $C_T \simeq N_T$ in the interfacial channel independently of the diffusion coefficient value. This renders the quantitative effect of hydrogen on interfacial cohesion insensitive to hydrogen diffusivity as it is the magnitude of C_T that determines the magnitude of Γ which is responsible for altering the cohesive properties. Perhaps the magnitude of the interfacial diffusivity may play a role in affecting the stress for void nucleation in materials with much lower interfacial binding energy. It should also be noted that in view of the very small occupancy of the NILS sites throughout the cell ($\theta_L \simeq 0.001\,76$), one by using equations (1)–(3), $\theta_T \simeq 1.0$, $\alpha = 1.0$, and $\beta = 1.0$ deduces that $C_T/C_L \simeq 10$ in the interfacial channel. This implies that most of the hydrogen in the interface gets trapped and therefore participates in the decohesion event. Looking at figures 9(c′) and 12 one may state that after an initial debond length is well formed, the magnitude of the interfacial diffusion constant has no effect on the debond propagation, as the distributions of hydrogen at low and large diffusivity look very much alike and the corresponding macroscopic stress–strain curves are the same.

Understanding the dependence of the plastic work expended during intergranular decohesion, γ_p, on the ideal work for brittle fracture 2γ is an issue first discussed by Rice (1966) thirty five years ago, and carefully elaborated by McMahon and Vitek (1979). McMahon and Vitek studied the effect of intergranular segregation of impurities on γ and in turn on γ_p through equation $d\gamma_p/\gamma_p = n\, d\gamma/\gamma$, in which $n \simeq 7.5$ is a multiplication factor which explains why a relatively small change in γ caused, for example, by impurity segregation to the grain boundaries may lead to a large change of γ_p and thus of the material fracture toughness. Extending this work, Jokl et al (1980) developed a Griffith type thermodynamic fracture criterion that accounts for the plastic work γ_p associated with dislocation emission from a crack tip over and above the work γ for bond stretching and breaking. In this paper, it has been demonstrated that when hydrogen affects interfacial cohesion, the energy absorbed by the unit cell reduces, only slightly though (figure 8). In the case of hydrogen-induced matrix softening this energy is reduced further. However, within this model assumptions, these macroscopic energy reductions are not dramatic enough for one to claim that the hydrogen effect changes the mode of fracture from macroscopically ductile to macroscopically brittle. Indeed, figure 8 shows that at macroscopic logarithmic strain $\varepsilon_{22} = 0.1$ one finds $dE_{tot}/E_{tot} \simeq n\, dE_{int}/E_{int}$ with $n \simeq 1$. This value of n is quite smaller than the value of 7.5 envisioned by McMahon and Vitek (1979). However, attention should be drawn to the fact that the values of E_{tot} and E_{int} may not be directly related to those of $\gamma + \gamma_p$ and γ in the work of McMahon and Vitek (1979) and Jokl et al (1980) since γ_p specifically denotes the work spent on localized shears within a few atomic spacings from the crack tip and it does not represent macroscopic work as $E_{tot} - E_{int}$ does in this work. The same comment applies to the relationship between γ

and E_{int}. Also it should be pointed out that the calculated value of n in this work pertains to decohesion taking place in plane-strain tension, i.e. at small hydrostatic stress whereas the suggestion of McMahon and Vitek (1979) pertains to debonding ahead of a crack tip, i.e. under high hydrostatic stress. Indeed, if tensile macroscopic stress σ_{11} were applied to the unit cell (which is the case of modeling decohesion at higher hydrostatic stresses), decohesion would happen at lower loads and that would prevent the specimen from deforming plastically in an extensive way. Such a decohesion scenario is currently being investigated.

8. Closure

The phenomenological model for interfacial decohesion of Liang and Sofronis (2003) that was calibrated at the fast-separation limit of the decohesion theory of Rice (1976), Hirth and Rice (1980), and Rice and Wang (1989) has been implemented in the set up of an initial/boundary-value problem at a unit cell for alloy 690. The finite element results account for the coupling between material elastoplasticity, hydrogen bulk and interfacial transport, and interfacial decohesion during the incremental solution of the coupled elastoplasticity and hydrogen transport equations. The simulation results may be summarized as follows:

(i) In the absence of softening, hydrogen reduces both the macroscopic stress and strain at which void nucleation takes place. Hydrogen-induced softening while it increases the nucleation strain, it further decreases the nucleation stress, though slightly. In addition, matrix softening due to hydrogen may be said that it embrittles the interface by reducing the energy expended both on macroscopic deformation and interfacial decohesion.

(ii) It is argued that the decohesion and hydrogen-enhanced localized plasticity mechanisms for hydrogen embrittlement should be viewed acting in synergism.

(iii) Stress elevation in the ligament between particles due to hydrogen-induced interfacial debonding enhances the corresponding local hydrogen accumulation. This can embrittle local grain boundaries and as a result, the mechanism of hydrogen assisted intergranular ductile fracture is a mechanism possible for alloy 690 decorated by grain boundary carbides.

(iv) The existing uncertainty on the magnitude of the interfacial diffusivity seems not to affect the predictions of the hydrogen population development when substantial decohesion has taken place. However, the magnitude of the interface diffusion coefficient does play a role on the hydrogen population development before void nucleation, but due to the high interfacial binding energy in this alloy no effect on void nucleation was detected.

(v) The interface is more resistant to decohesion at higher strain rates. This derives from the effect of strain rate on the transport process.

References

Bandyopadhyay N, Kameda J and McMahon C J Jr 1983 Hydrogen-induced cracking in 4340-type steel: effects of composition, yield strength, and H_2 pressure *Metall. Trans.* A **14** 881–8

Baranowski B, Majchrzak T B and Flanagan J 1971 The volume increase of f.c.c. metals and alloys due to interstitial hydrogen over a wide range of hydrogen contents *J. Phys. F: Metal Phys.* **1** 258–61

Birnbaum H K 1994 Hydrogen effects on deformation-relation between dislocation behavior and the macroscopic stress–strain behavior *Scr. Metall.* **31** 149–53

Birnbaum H K and Sofronis P 1994 Hydrogen-enhanced localized plasticity—a mechanism for hydrogen-related fracture *Mater. Sci. Eng.* A **176** 191–202

Bond G M, Robertson I M and Birnbaum H K 1987 The influence of hydrogen on deformation and fracture processes in high-strength aluminum alloys *Acta Metall.* **35** 2289–96

Bond G M, Robertson I M and Birnbaum H K 1988 Effects of hydrogen on deformation and fracture processes in high-purity aluminum *Acta Metall.* **36** 2193–7

Brown L M and Stobbs W M 1976 The work hardening of copper-silica—V. Equilibrium plastic relaxation by secondary dislocations *Phil. Mag.* **34** 351–72

Briant C L, Feng H C and McMahon C J Jr 1978 Embrittlement of a 5 pct nickel high strength steel by impurities and their effects on hydrogen-induced cracking *Metall. Trans.* A **9** 625–33

Chen X and Gerberich W W 1991 The kinetics and micromechanics of hydrogen assisted cracking in Fe-3 pct Si single crystals *Metall. Trans.* A **22** 59–70

Chen X, Foecke T, Lii M, Katz Y and Gerberich W W 1990 The role of stress state in Fe–Si single crystals *Eng. Fract. Mech.* **35** 997–1017

Chen S H, Katz Y and Gerberich W W 1991 Crack tip fields and fracture microplasticity in hydrogen-assisted cracking of Fe-3wt%Si single crystals *Phil. Mag.* **63** 131–55

Eastman J, Matsumoto T, Narita N, Heubaum N and Birnbaum H K 1981 Hydrogen effects in nickel embrittlement or enhanced ductility? *Hydrogen in Metals* ed I M Bernstein and A W Thompson (New York: Metallurgical Society of AIME) pp 397–409

Enmgelmann H J, Mummert K, Schwarz S and Uhlemann M 1995 Influence of cathodic and corrosive hydrogen on the cracking behavior of austenitic iron and nickel base alloys *Hydrogen Transport and Cracks in Metals* ed A Turnbull (Cambridge: Cambridge University Press) pp 27–37

Gerberich W W and Chen Y T 1975 Hydrogen-controlled cracking-an approach to threshold stress intensity *Metall. Trans.* A **6** 271–8

Gerberich W W and Foecke T J 1990 Hydrogen enhanced decohesion in Fe–Si single crystals: implications to modeling of thresholds *Hydrogen Effects on Materials Behavior* ed N R Moody and A W Thompson (Warrendale, PA: TMS) pp 687–701

Gerberich W W, Oriani R A, Lii M-J, Chen X and Foecke T 1991 The necessity of both plasticity and brittleness in the fracture thresholds of iron *Phil. Mag.* **63** 363–76

Gilman J J 1969 *Micromechanics of Flow in Solids* (New York: McGraw-Hill Book Company) pp 185–99

Goods S H and Brown L M 1979 The nucleation of cavities by plastic deformation *Acta Metall.* **27** 1–15

Govindarajan R M and Aravas N 1994 Deformation processing of metal powders. Part I—Cold isostatic pressing *Int. J. Mech. Sci.* **36** 343–57

Grove C A and Petzold L D 1985 Mechanisms of stress-corrosion cracking of alloy X-750 in high purity water *Corrosion of Nickel-Base Alloys* (PA: American Society for Metals) pp 165–80

Hirth J P 1990 Hydrogen influenced plastic instability and ductile fracture in steels *Hydrogen Effects on Material Behavior* ed N R Moody and A W Thompson (Warrendale, PA: TMS) pp 677–89

Hirth J P and Lothe J 1982 *Theory of Dislocations* (New York: Wiley)

Hirth J P and Rice J R 1980 On the thermodynamics of adsorption at interfaces as it influences decohesion *Metall. Trans.* A **11** 1501–11

Johnson H H and Lin R W 1981 Hydrogen and deuterium trapping in iron *Hydrogen Effects in Metals* ed I M Bernstein and A W Thompson (New York: Metallurgical Society of AIME) pp 3–23

Jokl M L, Vitek V and McMahon C J Jr 1980 A microscopic theory of brittle fracture in deformable solids: a relation between ideal work to fracture and plastic work *Acta Metall.* **28** 1479–88

Krom A H M, Koers R W J and Baker A 1999 Hydrogen transport near a blunting crack tip *J. Mech. Phys. Solids* **47** 971–92

Lessar J F and Gerberich W W 1976 Grain size effects in hydrogen-assisted cracking *Metall. Trans.* A **7** 953–60

Liang Y and Sofronis P 2003 Toward a phenomenological description of hydrogen-induced decohesion at particle/matrix interfaces *J. Mech. Phys. Solids* at press

Lufrano J, Sofronis P and Symons D 1998b Hydrogen transport and large strain elastoplasticity near a notch in alloy X-750 *Eng. Fract. Mech.* **59** 827–45

McMahon C J Jr 2001 Hydrogen-induced intergranular fracture of steels *Eng. Fract. Mech.* **68** 773–88

McMahon C J Jr and Vitek V 1979 The effects of segregated impurities on intergranular fracture energy *Acta Metall.* **27** 507–13

Mishin Y, Sofronis P and Bassani J L 2002 Thermodynamic and kinetic aspects of interfacial decohesion *Acta Mater.* **50** 3609–22

Morgan M J 1987 Grain boundary segregation and embrittlement by antimony and hydrogen in a model alloy steel *PhD Dissertation* University of Pennsylvania, Philadelphia, PA

Nagtegaal J C, Parks D M and Rice J R 1974 On numerically accurate finite element solutions in the fully plastic range *Comp. Meth. Appl. Mech. Eng.* **4** 153–77

Needleman A 1987 A continuum model for void nucleation by inclusion debonding *J. Appl. Mech.* **54** 525–31

Needleman A and Xu X-P 1993 Void nucleation by inclusion debonding in a crystal matrix *Model. Simul. Mater. Sci. Eng.* **1** 111–32

Onyewuenyi O A and Hirth J P 1982 Plastic instability in U-notched bend specimens of spheroidized AISI 1090 steel *Metall. Trans.* A **13** 2209–18

Onyewuenyi O A and Hirth J P 1983 Effects of hydrogen on notch ductility and fracture in spheroidized AISI 1090 steel *Metall. Trans.* A **14** 259–69

Oriani R A 1970 The diffusion and trapping of hydrogen in steel *Acta Metall.* **18** 147–57

Oriani R A and Josephic P H 1974 Equilibrium aspects of hydrogen-induced cracking of steels *Acta Metall.* **22** 1065–74

Oriani R A and Josephic P H 1977 Equilibrium and kinetic studies of the hydrogen-assisted cracking of steel *Acta Metall.* **25** 979–88

Oriani R A and Josephic P H 1979 Hydrogen enhanced load relaxation in a deformed medium-carbon steel *Acta Metall.* **27** 997–1005

Peisl H 1978 Lattice strains due to hydrogen in metals *Hydrogen in Metals I, Topics in Appl. Phys.* **28** 53–74

Rajan V B and Hirth J P 1987 Effect of hydrogen on four-point bend tests of U-notched AISI 1090 steel *Metall. Trans.* A **18** 335–40

Rice J R 1966 An examination of the fracture mechanics energy balance from the point of view of continuum mechanics *Proc. 1st International Conf. on Fracture (Sendai, Japan)* ed T Yokobori *et al*, pp 309–40

Rice J R 1976 Hydrogen and interfacial cohesion *Effect of Hydrogen on Behavior of Materials* (New York: TMS-AIME) pp 455–66

Rice J R and Wang J-S 1989 Embrittlement of interfaces by solute segregation *Mater. Sci. Eng.* A **107** 23–40

Robertson I M and Birnbaum H K 1986 An HVEM study of hydrogen effects on the deformation and fracture of nickel *Acta Metall.* **34** 353–66

Robertson I M 2001 The effect of hydrogen on dislocation dynamics *Eng. Fract. Mech.* **68** 671–92

Rozenak P, Robertson I M and Birnbaum H K 1990 HEVM studies of the effects of hydrogen on the deformation and fracture of AISI type 316 austenitic stainless steel *Acta Metall.* **38** 2031–40

Sato A and Meshii M 1973 Solid solution softening and solid solution hardening *Acta Metall.* **21** 753–68

Sofronis P and Birnbaum H K 1995 Mechanics of the hydrogen-dislocation-impurity interaction—I. Increasing shear modulus *J. Mech. Phys. Solids* **43** 49–90

Sofronis P and McMeeking R M 1989 Numerical analysis of hydrogen transport near a blunting crack tip *J. Mech. Phys. Solids* **37** 317–50

Sofronis P, Liang Y and Aravas N 2001 Hydrogen induced shear localization in metals and alloys *Eur. J. Mech. A-Solids* **20** 857–72

Symons D and Thomspon A W 1996 The effect of hydrogen on the fracture of alloy X-750 *Metall. Trans.* A **27** 101–10

Symons D and Thomspon A W 1997 The effect of hydrogen on the fracture toughness of alloy X-750 *Metall. Trans.* A **28** 817–23

Symons D 1998 The effect of carbide precipitation on the hydrogen-enhanced fracture behavior of alloy 690 *Metall. Trans.* A **29** 1265–77

Symons D 2001 A comparison of internal hydrogen embrittlement and hydrogen environment embrittlement of X-750 *Eng. Fract. Mech.* **68** 751–71

Tabata T and Birnbaum H K 1983 Direct observations of the effect of hydrogen on the behavior of dislocations in iron *Scr. Metall.* **17** 947–50

Tabata T and Birnbaum H K 1984 Direct observations of hydrogen enhanced crack propagation in iron *Scr. Metall.* **17** 947–50

Takeda Y and McMahon C J Jr 1981 Strain controlled vs stress controlled hydrogen induced fracture in a quenched and tempered steel *Metall. Trans.* A **12** 1255–66

Teter D F, Robertson I M and Birnbaum H K 2001 The effects of hydrogen on the deformation and fracture of beta-titanium *Acta Mater.* **49** 4313–23

Thomas G J 1989 Hydrogen trapping in FCC metals *Hydrogen Effects in Metals: Proc. 3rd International Conf. on Effect of Hydrogen on Behavior of Materials* ed I M Bernstein and A W Thompson (New York: The Metallurgical Society of AIME) pp 77–84

Thompson A W and Knott J F 1993 Micromechanisms of brittle fracture *Metall. Trans.* A **24** 523–34

Tobe Y and Tyson W R 1977 Effect of hydrogen on yield of iron *Scr. Met.* **11** 849–52

Tvergaard V 1990 Effect of fiber debonding in a whisker-reinforced metal *Mater. Sci. Eng.* A **125** 203–13

Tvergaard V and Hutchinson J W 1993 The influence of plasticity on mixed mode interface toughness *J. Mech. Phys. Solids* **41** 1119–35

Unger D J 1989 A mathematical analysis for impending hydrogen assisted crack propagation *Eng. Fract. Mech.* **34** 657–67

Van Leeuwen H P Van 1974 The kinetics of hydrogen embrittlement: a quantitative diffusion model *Eng. Fract. Mech.* **6** 141–61

Xu Y and Bassani J L 1999 A steady state model for diffusion-controlled fracture *Mater. Sci. Eng.* A **260** 48–54

Yao J and Cahoon J R 1988 Diffusion of hydrogen induced grain boundary fracture in high purity nickel and its alloys-enhanced hydrogen diffusion along grain boundaries *Scr. Metall.* **22** 1817–20

Young G A and Scully J R 1997 Evidence that carbide precipitation produces hydrogen traps in Ni–17Cr–8Fe alloys *Scr. Metall.* **36** 713–19